Superfluidity of Helium-4 Films on Graphene Substrate

by

Sam Yu

A thesis submitted in partial fulfillment of the requirements
for the degree of

Master of Science

Department of Physics
University of Alberta

Abstract

We study the ground state physics of a helium-4 monolayer adsorbed onto graphene substrate through means of quantum Monte Carlo simulations. At low temperatures, helium-4 is well-known to undergo a superfluid transition. In the presence of a modulating potential from corrugated substrates like graphene however, the situation is less clear. This thesis is primarily aimed at addressing existing controversy in the literature about whether a metastable superfluid state exists when the system is a commensurate $C_{1/3}$ crystal. Starting from a detailed microscopic model, we conduct first principles quantum Monte Carlo simulations of the system at both finite and zero temperature. Our results indicate the absence of a superfluid signal in the ground state crystal, with no evidence of a low-lying fluid state.

Preface

The work presented in this thesis constitutes the original research of Sam Yu under the supervision of Professor Massimo Boninsegni. The main physical results of the research work described here, mainly presented in Chapter 3, are summarized in a manuscript that has been submitted for publication to *Communications in Theoretical Physics*. It is available in the ArXiv public repository (https://arxiv.org/abs/2403.02033).

Acknowledgements

As my time as a graduate student at the University of Alberta approaches its end, there are several people I would like to acknowledge whose support was instrumental towards the successful and rewarding completion of my degree.

First off, I would like to extend my deep gratitude to my supervisor, Professor Massimo Boninsegni for his continuous support throughout my masters. Navigating through academia is daunting as a newcomer, so I am fortunate to have had such a supportive and dedicated supervisor guiding me throughout. Many times I came to his office confused about my results or direction, and I have always left with more clarity thanks to his wisdom. His keen physical intuition and commitment to simplicity have been inspiring towards my growth as a scientist.

I would also like to thank the other members of my supervisory committee: Professor Igor Boettcher, Professor Nassim Bozorgnia, and Professor Frank Marsiglio for their valuable feedback on my project and thesis, which helped me improve the quality of my thesis writing and gave me interesting questions to mull over that I had not considered before. I would like to give special thanks to Professor Igor Boettcher in particular for hosting the weekly CMP/TPI seminars and for involving me in his research on superfluid helium-3, which gave me the opportunity to learn more about condensed matter field theory and the fascinating physics of helium-3. When I was working on this project, Dr. Canon Sun graciously answered my numerous questions about helium-3 and field theory, which I am very thankful for.

I gratefully acknowledge financial support from the Alberta Graduate Excellence Scholarship (AGES) and the University of Alberta Recruitment Scholarship, which

helped me worry less about my financial stability, as well as the computing resources provided by the Digital Alliance of Canada which performed the many, many Monte Carlo calculations in this work.

Finally, completing my degree would not have been possible without the support from the amazing friends I made in Edmonton: Albion - for your intellectual curiosity and dry European humor, Max - for always spicing up the outings and your surreal, off-beat sense of humor, Mubasher - for your level-headedness, and generally being a beast in quantum field theory and tennis, Shafakat - for hosting all those game nights, being my gym buddy, and always having something funny to share, Rishap - for always being an awesome host and inspiring me with your diverse set of interests, Abhinab - for all the times you drove us around and the late night deep conversations we had, Kusum - for your unconditional kindness, support, and empathy throughout all the good and bad during my masters.

This also goes out to my wonderful friends and family back in Toronto: my mother, my father, grandpa, grandma, my brother, Daniel, Yusuf, Christa, Zara, and Franky.

Table of Contents

List of Figures

Chapter 1

Introduction

Quantum mechanics (QM) is one of the most successful theories in physics, describing physical phenomena taking place at atomic and molecular scales. Despite its famously non-intuitive nature, the utility of QM cannot be overstated as many of its predictions are undoubtedly in amazing agreement with experiment. Several major technological advances in the twentieth century would not be possible without QM, such as the invention of the transistor, heralding in the age of computers.

Given that QM is such a successful theory, there are now two distinct lines of inquiry one may take given QM as their bedrock. The first route would be to ask what physics takes place at even smaller length scales than molecules and atoms. Are the protons, neutrons, and electrons which make up an atom composed of even smaller, more fundamental constituents? The wave-like properties of particles in QM are emphasized by the de-Broglie relation $\lambda = h/p$ where λ is the particle's de-Broglie wavelength and p is its momentum. Therefore, collisions in scattering experiments must occur within highly relativistic regime of energies, which is needed to provide sufficient spatial resolution for observing more fundamental particles in the collision products. Investigations along this line mean that quantum theory has to be reconciled with Einstein's theory of special relativity, which led to the development of quantum field theory (QFT) and the Standard Model of elementary particles in the second half of the twentieth century.

On the other hand, one can think of larger scale structure and consider what happens when systems of interacting quantum particles are put together, which can range from a few particles or macroscopically many in the thermodynamic limit. This is the quantum many-body problem and a subject of *condensed matter physics*. It is a very hard problem in general due to the exponential scaling of the Hilbert space's size with the number of particles, with strong interactions rendering it impossible to utilize perturbation theory.

However, in spite of the problem's sheer complexity, great progress has been made towards the development of computational methods, which prove highly useful when analytical approaches fail. Interest in such methods has been growing in tandem with increasing computing power over the years. One method in particular, quantum Monte Carlo (QMC), has been indispensable towards the study of systems of bosons, allowing one to compute their thermodynamic properties accurately and produce theoretical predictions that are readily comparable to experiment. A great advantage of quantum Monte Carlo is its flexibility; if one can write down the quantum-mechanical Hamiltonian describing a many-body system, then there's a good chance that it is applicable, with some notable exceptions[1].

Superfluidity, an example of a macroscopic quantum phenomenon, is one fascinating character of Bose systems which can be readily studied with quantum Monte Carlo. Certain substances acquire superfluid properties at low temperatures and become capable of flowing frictionlessly without dissipation of their kinetic energy. Elucidating the nature of superfluidity is of marked interest to theorists and experimentalists because of its connection with superconductivity, as the current in a superconductor can be thought of as a charged superfluid.

The first substance discovered to have superfluid properties was liquid helium-4 by Kapitza [1] in 1937, as well as independently by Allen and Misner [2] in the same year, its superfluid phase occurring when it is cooled below a critical temperature of

---

[1] Systems of fermions, as we will see later in this thesis.

$T_\lambda = 2.17\,K$. The substance remains a liquid all the way down to zero temperature, as the zero-point motion of its atoms is enough to overcome the weak interatomic interactions and disrupt the formation of a crystal. Helium-3 on the other hand, can also become a superfluid, albeit at a much lower temperature of $\sim 1\,\mathrm{mK}$. This is due to the fact that before transitioning to the superfluid phase, helium-3 atoms pair up to form composite bosons called Cooper pairs, while the helium-3 atoms by themselves are fermions owing to the spins of their nuclei. The Cooper pairing mechanism underlying the superfluid transition of helium-3 demonstrates an intriguing connection between superfluidity and Bose-Einstein condensation.

Due to the structural simplicity of helium-4 atoms, which can be regarded as point-like bosonic particles, they provide a convenient testbed for simulating more exotic kinds of superfluids, such as those occurring in lower dimensions. The dimensionality of the space is fundamentally important to condensed matter physicists, as it sets the stage for exotic phases of matter that only emerge in lower dimensions. One striking example is that of anyonic quasiparticle excitations, which only exist in two dimensions and exhibit *parastatistics*: the many-body wavefunction acquires a complex phase $e^{i\theta}$ when any two anyons are exchanged, as opposed to the more traditional quantum statistics obeyed by bosons and fermions in 3D.

An experimentally convenient way of engineering effectively 2D systems is through adsorbing its constituents onto attractive substrates, with a range of different behaviors exhibited depending on the kind that is used. For example, when helium-4 atoms are adsorbed onto weakly-binding substrates such as lithium, a superfluid film is formed whose thickness grows continuously as a function of the chemical potential [3–5]. Another commonly studied substrate is graphite, which is one of the most strongly attractive substrates available. An allotrope of carbon, it is made up of several graphene layers stacked on top of each other and held together by van der Waals forces, each graphene sheet comprising of carbon atoms arranged into a honeycomb lattice. When adsorbed onto graphite substrate at low densities, helium-4 atoms form an atomically-thin monolayer over the graphite [6–9]. As more helium atoms are successively adsorbed, multiple distinct layers can be formed, each constituting essentially independent 2D systems [10–12]. At low temperatures, helium-4 films on graphite exhibit a variety of different crystal phases, both commensurate and incommensurate with respect to the graphite lattice. The first two helium-4 layers are known to be crystalline upon completion [13], while the third layer and beyond are superfluid [11, 14]. By stacking up enough layers, one can study the transition of the system's physics from two to three dimensions.

In general, helium films on graphite provide a flexible platform for realizing a variety of condensed matter systems, arising from the ability for the graphite surface to be preplated. For example, preplating the substrate with helium-4 before subsequent adsorption of helium-3 allows for the study of 2D Fermi systems. If the graphite is first preplated with a solid helium-4 bilayer to create a composite substrate, then the adsorbed helium-3 bilayer film on top will exhibit heavy fermion behavior and quantum criticality [15–17]. A helium-3 fluid film grown over graphite preplated with a deuterium or helium-4 monolayer exhibits a density-tuned Mott transition [18, 19]. Solid helium-3 monolayers on graphite on the hand yield a playground for examining two-dimensional frustrated magnets [20–22].

Another fascinating state of matter which can be potentially manifested is a 2D 'supersolid', where the helium atoms crystallize over the graphite, yet quantum exchanges between atoms in different crystal sites permit a global superfluid response. Although this is not a true supersolid phase [23] because translational symmetry is broken by an external modulating potential rather than through interatomic interactions alone, such a phase would be intriguing since it combines two seemingly contradictory properties. Following reports of a non-classical moment of inertia in solid helium-4 from torsional oscillator experiments conducted by Kim and Chan [24], considerable attention has been dedicated towards the search for supersolidity in helium-4 crystals from first-principles computational studies with QMC. However, previous numerical studies of the first and/or second helium layer over graphite have not found evidence of such a phenomenon [25], unless the helium crystal is doped with vacancies [26].

A graphene sheet by itself has a somewhat weaker (∼10%) attraction than graphite [27], but otherwise, the graphene-induced potential landscape has essentially the same corrugation as that from a graphite substrate. Previous QMC calculations [26, 28] show that, despite the reduced binding energy, the equilibrium crystal phases for the first two helium layers on graphene are identical to those found for graphite [25].

It is generally accepted that a helium-4 monolayer has an equilibrium $C_{1/3}$ crystal phase on graphene at an areal density of $0.0636\,\mathring{A}^{-2}$, wherein one third of the hexagonal centers are occupied by a helium atom. There is some controversy however, about whether a superfluid signal exists in this state that can be detected experimentally, as several groups have made conflicting predictions, with some finding no evidence of superfluidity [28], others finding a small yet finite fraction [26], or a long-lived, metastable liquid that is energetically competitive with the solid phase [27].

The goal of this thesis is to address this controversy by conducting our own quantum Monte Carlo simulations of a helium monolayer on top of graphene, starting from a realistic, microscopic model of the system. The remainder of this thesis is organized as follows. First, the methodology of quantum Monte Carlo is introduced after a brief review of the path integral formulation of quantum statistical mechanics. The effects of particle indistinguishability and differences between finite-temperature and zero-temperature methods are elaborated upon. Estimators for the energy, pair correlation function, structure factor, and superfluid fraction are then derived. Finally, we apply the developed methodology to analyze the superfluid content of a helium monolayer film adsorbed onto graphene and outline our conclusions.

Chapter 2

Background

We will now describe the computational methodology we utilize for performing the calculations in this thesis. As a road-map for how this chapter is structured, in Section 2.1 we formulate quantum statistical mechanics in terms of imaginary-time path integrals, necessitating the evaluation of very high-dimensional integrals to obtain expectation values. In Section 2.2, we show how to evaluate these integrals through Monte Carlo methods. In Section 2.3, we incorporate the effects of particle indistinguishability into our methodology through a permutation sampling scheme. In Section 2.4, we discuss two important zero-temperature variants of quantum Monte Carlo: Diffusion Monte Carlo (DMC) and Path Integral Ground State (PIGS), which are important towards the methodological aspects of our work on the helium-graphene problem. Finally, in Sections 2.5 and 2.6 we derive estimators for physical observables and consider a few details regarding the computational implementation of our methodology. All of the energies we will report are related to the temperature parameter of our simulations via proportionality constant k_B. Henceforth, for the remainder of this thesis we shall set $k_B = 1$ so that all energies are expressed in units of Kelvin.

2.1 Path Integral Formulation of Quantum Statistical Mechanics

We will begin by briefly reviewing some foundational concepts from quantum statistical mechanics. Consider a system of N particles in thermal equilibrium with a heat bath at temperature T. It is a fundamental result from quantum statistical mechanics that the system's state $\hat{\rho}$ is described by the *thermal density matrix*

$$\hat{\rho} = e^{-\beta\hat{H}}/Z \tag{2.1}$$

where $Z = \mathrm{Tr}\left(e^{-\beta\hat{H}}\right)$ is called the *partition function* and $\beta = T^{-1}$ is the inverse temperature. The thermal expectation value of any observable $\hat{O}$ characterizing the system is given by

$$\left\langle\hat{O}\right\rangle = \mathrm{Tr}\left(\hat{\rho}\hat{O}\right) \tag{2.2}$$

which is the primary quantity that quantum Monte Carlo aims to calculate.

For now, let us treat the particles as distinguishable. The positions of all particles can be written into a single many-body position as $\mathbf{R} = \mathbf{r}_1 \cdots \mathbf{r}_N$, such that $|\mathbf{R}\rangle$ is the state constructed from the tensor product of position eigenstates $|\mathbf{r}_i\rangle$ for individual particles, the set of which $\{|\mathbf{R}\rangle\}$ provides an orthonormal basis of the joint Hilbert space for expanding the trace

$$\left\langle\hat{O}\right\rangle = Z^{-1}\int \mathrm{d}\mathbf{R}\,\langle\mathbf{R}|\,e^{-\beta\hat{H}}\hat{O}\,|\mathbf{R}\rangle = \frac{\int \mathrm{d}\mathbf{R}\,\mathrm{d}\mathbf{R}'\,\rho(\mathbf{R},\mathbf{R}';\beta)\,\langle\mathbf{R}'|\,O\,|\mathbf{R}\rangle}{\int \mathrm{d}\mathbf{R}\,\rho(\mathbf{R},\mathbf{R},\beta)} \tag{2.3}$$

where the *imaginary time propagator* is defined as

$$\rho(\mathbf{R},\mathbf{R}';\beta) \equiv \langle\mathbf{R}|\,e^{-\beta\hat{H}}\,|\mathbf{R}'\rangle \tag{2.4}$$

If $\beta = it/\hbar$, then the operator exponential would just be the ordinary time evolution operator over time t. Thus, it is said that $\rho(\mathbf{R},\mathbf{R}';\beta)$ gives the probability amplitude of transitioning from state $|\mathbf{R}'\rangle$ to $|\mathbf{R}\rangle$ over the 'imaginary time' interval $\beta\hbar$, hence the moniker.

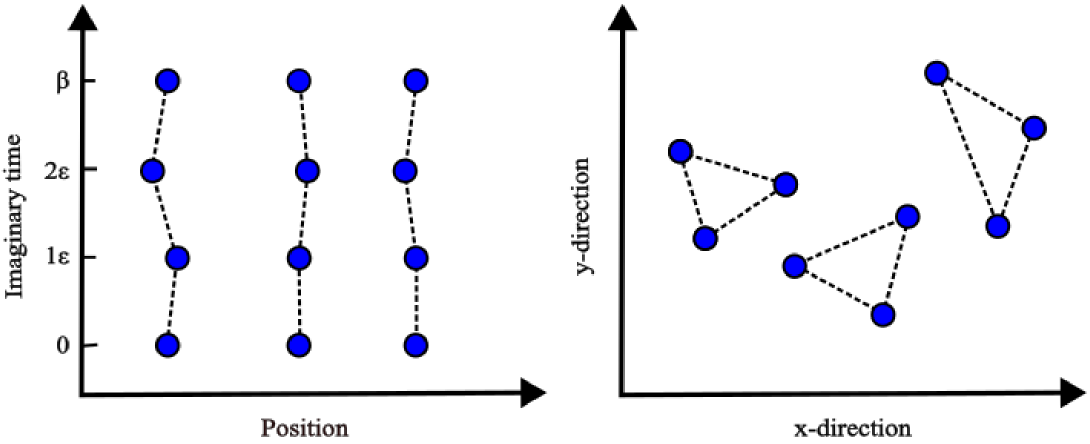

Figure 2.1: Schematic depiction of a configuration $\boldsymbol{X}$ containing the world lines of $N = 3$ particles with Trotter number $M = 3$. *Left:* Vertical axis is taken to be imaginary time so that the β-periodicity is manifest. *Right:* Particle world lines in imaginary time with both axes representing the spatial dimensions. β-periodicity in imaginary time implies that the world lines are closed: they are 'ring polymers'.

To proceed, it is useful to write Eqs. (2.4) and (2.3) as path integrals through a procedure called *time-slicing*. This follows by first noting $e^{-\beta \hat{H}} = (e^{-\epsilon \hat{H}})^M$ where $\beta = M\epsilon$ and M is called the *Trotter number*. Then, by inserting $M-1$ resolutions of the identity $\mathbb{1} = \int \mathrm{d}\mathbf{R} \, |\mathbf{R}\rangle \langle \mathbf{R}|$, we get

$$\begin{aligned}\rho(\mathbf{R}, \mathbf{R}'; \beta) &= \int \mathrm{d}\mathbf{R}_1 \cdots \mathrm{d}\mathbf{R}_{M-1} \, \langle \mathbf{R}| \, e^{-\epsilon \hat{H}} \, |\mathbf{R}_1\rangle \cdots \langle \mathbf{R}_{M-1}| \, e^{-\epsilon \hat{H}} \, |\mathbf{R}'\rangle \\ &= \int \mathrm{d}\mathbf{R}_1 \cdots \mathrm{d}\mathbf{R}_{M-1} \prod_{j=0}^{M-1} \rho(\mathbf{R}_j, \mathbf{R}_{j+1}; \epsilon) \end{aligned} \tag{2.5}$$

where $\mathbf{R} = \mathbf{R}_0$ and $\mathbf{R}_M = \mathbf{R}'$. The propagator is given by the sum over all possible "discretized" many-particle trajectories connecting $\mathbf{R}$ and $\mathbf{R}'$. We can do the same for the partition function and obtain

$$Z = \int \mathrm{d}\mathbf{R} \, \rho(\mathbf{R}, \mathbf{R}; \beta) = \int \mathrm{d}\mathbf{R}_0 \mathrm{d}\mathbf{R}_1 \cdots \mathrm{d}\mathbf{R}_{M-1} \prod_{j=0}^{M-1} \rho(\mathbf{R}_j, \mathbf{R}_{j+1}; \epsilon) \tag{2.6}$$

where now $\mathbf{R} = \mathbf{R}_0 \equiv \mathbf{R}_M$. Thus, the partition function is calculated by summing over all possible closed many-particle trajectories in the path integral formalism. Alternatively, Eqs (2.5) and (2.6) could have been obtained as a consequence of the propagator's convolutional property

$$\rho(\mathbf{R},\mathbf{R}';\beta_1+\beta_2) = \int \mathrm{d}\mathbf{R}''\,\rho(\mathbf{R},\mathbf{R}'';\beta_1)\rho(\mathbf{R}'',\mathbf{R}';\beta_2) \tag{2.7}$$

For ease of notation, from now on let us denote the *world line configuration* $\mathbf{X} = \mathbf{R}_0\mathbf{R}_1\cdots\mathbf{R}_M$ as a collection of time slices ordered according to imaginary time, representing a β-periodic many-particle path in imaginary time. A schematic depiction of a world line configuration is given in Fig. 2.9.

Now, the thermal expectation value of any observable $\hat{O}$ can be recast as the integral of some weight function $w(\mathbf{X})$ (that is associated with $\hat{O}$) with respect to a probability distribution $\pi(\mathbf{X})$ over the space of paths

$$\left\langle \hat{O} \right\rangle = \int \mathrm{d}\mathbf{X}\,\pi(\mathbf{X})w(\mathbf{X}) \tag{2.8}$$

where the probability distribution is given by

$$\pi(\mathbf{X}) = \frac{\prod_{j=0}^{M-1}\rho(\mathbf{R}_j,\mathbf{R}_{j+1};\epsilon)}{\int \mathrm{d}\mathbf{X}\prod_{j=0}^{M-1}\rho(\mathbf{R}_j,\mathbf{R}_{j+1};\epsilon)} \tag{2.9}$$

over the space of closed world line configurations, i.e. $\mathbf{R}_0 \equiv \mathbf{R}_M$ in $\mathbf{X}$. If $\hat{O}$ is a function of only the particle coordinates, i.e. it is a structural observable, then $\langle\mathbf{R}|\,\hat{O}\,|\mathbf{R}'\rangle = O(\mathbf{R})\delta(\mathbf{R}-\mathbf{R}')$, which implies $w(\mathbf{X}) = O(\mathbf{R}_k)$. Due to the cyclical property of trace, any time slice $\mathbf{R}_k$ of $\mathbf{X}$ can be chosen as the argument to the weight function, such as the middle time slice $\mathbf{R}_{M/2}$. Inspecting Eq. (2.9), calculating thermal expectation values requires the evaluation of a very high-dimensional integral over a total of $3NM$ coordinates. We will tackle the computation using the Monte Carlo methods discussed in Section 2.2.

The primary benefit of converting to a path integral representation is that thermal expectation values are now expressed in terms of "short-time" propagators $\rho(\mathbf{R},\mathbf{R}';\epsilon)$. To this end, let us assume that the Hamiltonian describing the system is separable into a kinetic term, as well as a potential term that is only a function of position: $\hat{H} = \hat{K} + \hat{V}$. In position space, it is given by

$$\mathcal{H} = -\lambda\sum_{i=1}^{N}\nabla_i^2 + V(\mathbf{R}) \tag{2.10}$$

where $\lambda = \hbar^2/2m$ and m is the mass of the particle species considered. The strategy then is to exploit the smallness of parameter ϵ by substituting some perturbative approximation for $\rho(\mathbf{R}, \mathbf{R}'; \epsilon)$. The most commonly known approximation is the *primitive approximation*, which arises from applying the Suzuki-Trotter formula

$$e^{-\epsilon \hat{H}} = e^{-\epsilon \hat{K}} e^{-\epsilon \hat{V}} + \mathcal{O}(\epsilon^2) \tag{2.11}$$

We substitute this expression into Eq. (2.4) and insert a complete set of position eigenstates between the exponentials. Evaluating the integral yields the short-time propagator

$$\rho(\mathbf{R}, \mathbf{R}'; \epsilon) = \rho_F(\mathbf{R}, \mathbf{R}'; \epsilon) e^{-\epsilon V(\mathbf{R}')} + \mathcal{O}(\epsilon^2) \tag{2.12}$$

in the primitive approximation, where

$$\rho_F(\mathbf{R}, \mathbf{R}'; \epsilon) = \langle \mathbf{R} | \, e^{-\epsilon \hat{K}} \, | \mathbf{R}' \rangle \tag{2.13}$$

is the propagator for a system of free particles, i.e. an ideal gas. For an ideal gas, the momenta of the particles are good quantum numbers. Therefore, it is convenient to insert a complete set of eigenstates $\{|\boldsymbol{P}\rangle\}$ of the operator $\hat{\boldsymbol{P}}$ (which collects the momenta of each particle) into Eq. (2.13). Since the momentum eigenstates are plane waves in position space, Eq. (2.13) becomes the Fourier transform of a Gaussian. Evaluating the transform gives

$$\rho_F(\mathbf{R}, \mathbf{R}'; \epsilon) = \frac{1}{(4\pi\lambda\epsilon)^{3N/2}} e^{-\frac{(\mathbf{R}-\mathbf{R}')^2}{4\lambda\epsilon}} \tag{2.14}$$

which is again a Gaussian. The full propagator in the primitive approximation is then

$$\rho(\mathbf{R}, \mathbf{R}'; \beta) \propto \int \mathrm{d}\mathbf{R}_1 \cdots \mathbf{R}_{M-1} \exp\left(-\sum_{j=0}^{M-1} \left[\frac{(\mathbf{R}_{j+1} - \mathbf{R}_j)^2}{4\lambda\epsilon} + \epsilon V(\mathbf{R}_{j+1}) \right] \right) \tag{2.15}$$

By taking the continuum limit ($M \to \infty$) we get

$$Z = \int \mathrm{d}\mathbf{R} \, \rho(\mathbf{R}, \mathbf{R}; \beta) \propto \int \mathrm{D}\mathbf{R}(\tau) \; e^{-S_E[\mathbf{R}(\tau)]/\hbar} \tag{2.16}$$

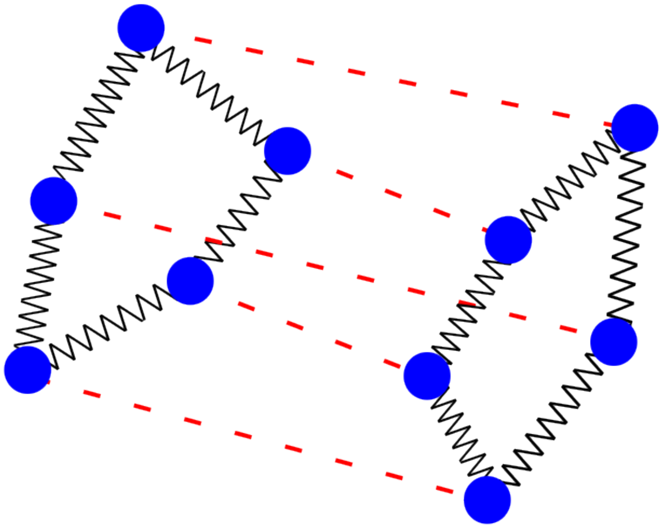

Figure 2.2: System of two ring polymers with beads connected with springs, and an 'iso-time' potential coupling together beads on the same time slice (shown as the red dotted lines). The larger that the particle masses are, the stiffer the springs, reducing the polymer sizes. In the world-line picture, the size is a measure of the particle's quantum delocalization. Thus, larger masses imply that the system behaves more classically.

where D**R** is an integration measure summing over all closed imaginary time paths and S_E is called the *Euclidean action*, given by

$$S_E[\mathbf{R}(\tau)] = \int_0^{\beta\hbar} \mathrm{d}\tau \left(\sum_{i=1}^{N} \frac{m}{2} \left(\frac{\mathrm{d}\mathbf{R}_i}{\mathrm{d}\tau} \right)^2 + V(\mathbf{R}) \right) \tag{2.17}$$

Based on Eq. (2.16), the imaginary time paths which minimize the action will contribute the most to the partition function. The first term in Eq. (2.17) represents the kinetic energy in imaginary time and favors paths which have less curvature. On the other hand, the potential energy term favors localizing the world lines within regions of lower potential energy, which necessarily induces curvature in the paths for them to occupy a restricted volume. Therefore, the shapes of the imaginary time world lines in $\mathbf{R}(\tau)$ are dictated by the competition between the kinetic and potential terms in the action.

Interestingly, it should be noted that the partition function given in Eq. (2.16) with M finite exactly corresponds to the partition function of a classical system of polymers with beads connected by springs with spring constant $(4\lambda\epsilon)^{-1}$, albeit, with a peculiar "iso-time" interaction potential between polymers only acting between beads on the same time slice. Keeping this correspondence in mind, we often refer to positions along world lines as "beads" and the single-particle propagators connecting positions along world lines as "links". A depiction of a two polymer system is shown in Fig. 2.2.

The primitive approximation (Eq. (2.12)) is the simplest approximation available for the short-time propagator, having a error term that is quadratic in ϵ at leading order. For better performance, one may use higher-order approximations of the short-time propagator. For example, a second-order "Trotterization" of $e^{-\epsilon\hat{H}} = e^{-\epsilon(\hat{K}+\hat{V})}$ is given by

$$e^{-\epsilon\hat{H}} = e^{-\epsilon\hat{V}/2}e^{-\epsilon\hat{K}}e^{-\epsilon\hat{V}/2} + \mathcal{O}(\epsilon^3) \tag{2.18}$$

Substituting into Eq. (2.4), we obtain the following short-time propagator

$$\rho_3(\mathbf{R},\mathbf{R}';\epsilon) = e^{-\epsilon(V(\mathbf{R})+V(\mathbf{R}'))/2}\rho_F(\mathbf{R},\mathbf{R}';\epsilon) + \mathcal{O}(\epsilon^3) \tag{2.19}$$

For the calculations performed in this thesis, we use the following fourth-order approximation for the propagator taken from Refs. [29, 30]:

$$\begin{aligned} \rho_4(\mathbf{R}_j,\mathbf{R}_{j+1};\epsilon) &= \rho_F(\mathbf{R}_j,\mathbf{R}_{j+1};\epsilon)\exp(-\epsilon U(\mathbf{R}_j)) \\ U(\mathbf{R}_j) &= \frac{2V(\mathbf{R}_j)}{3} + \tilde{V}(\mathbf{R}_j) \\ \tilde{V}(\mathbf{R}_j) &= \begin{cases} \frac{2V(\mathbf{R}_j)}{3} + \frac{2\lambda\epsilon^2}{9}\sum_{i=1}^{N}(\nabla_i V(\mathbf{R}_j))^2 & \text{j is odd} \\ 0 & \text{j is even} \end{cases} \end{aligned} \tag{2.20}$$

High-order approximations with errors better than or equal to $\mathcal{O}(\epsilon^5)$ can also be obtained [31, 32], but tend to be difficult to implement because they involve complicated expressions with layers of nested commutators between $\hat{K}$ and $\hat{V}$ or problematic negative imaginary-time terms. Thus, fourth-order propagators are most commonly used in the algorithms of present day studies.

2.2 The Monte Carlo Method

In order to calculate thermal expectation values, we must calculate very high dimensional integrals over the system's configuration space. This is not surprising, given the rapid scaling of microscopic degrees of freedom with the number of particles in our system. It turns out that the problem of computing expectation values lends itself naturally to *Monte Carlo* methods, which are stochastic methods that were first pioneered by scientists at Los Alamos Laboratory during the Second World War for calculating neutron diffusion out of the cores of thermonuclear weapons [33]. The moniker 'Monte Carlo' was coined by physicist Stanislaw Ulam, one of the main developers of the method. It arose from the need for a secret code name for the project and derives from the Monte Carlo casino in Monaco, inspired by the gambling habits of Ulam's uncle. In this section, we will introduce the Monte Carlo method as a means for evaluating high-dimensional integrals, drawing from Ref. [34].

2.2.1 Monte Carlo Integration

One of the simplest manifestations of a Monte Carlo method is for integrating single-variable functions. Suppose we want to numerically evaluate $I = \int_a^b \mathrm{d}x\, f(x)$ for some well-behaved function $f(x)$. Typically, one integrates f(x) numerically through quadrature: by taking equally spaced points over the interval and constructing a Riemann sum. Another way is through sampling N uniformly-random points x_i over the interval and evaluating the Monte Carlo estimator

$$\tilde{I}(N) = \frac{(b-a)}{N} \sum_{i=1}^{N} f(x_i) \approx I \tag{2.21}$$

which is stochastic by nature. However, it can be shown $\tilde{I}(N)$ is an unbiased estimator, i.e. its expected value exactly equals I. The proof follows from the fact that $\langle f(x_i) \rangle = \frac{1}{b-a} \int_a^b f(x)\, \mathrm{d}x$ for all $1 \leq i \leq N$, i.e. the expected value of $f(x_i)$ is simply its average value over the interval. By linearity of expectation, we have

$$\left\langle \tilde{I}(N) \right\rangle = \frac{(b-a)}{N} \sum_{i=1}^{N} \langle f(x_i) \rangle = I \tag{2.22}$$

as expected. To assess the error in $\tilde{I}(N)$, we want an idea of the dispersion of $\tilde{I}(N)$ about its expected value. By computing the variance in the estimator, it is found that

$$\sigma^2 = \left\langle I^2 \right\rangle - \langle I \rangle^2 = \alpha N^{-1} \tag{2.23}$$

where α is a constant dependent on a, b, and f but not on N. In other words, the characteristic length scale for fluctuations of $\tilde{I}(N)$ away from I is $\propto N^{-1/2}$. On the other hand, for standard numerical integration (quadrature) involving equidistant values of x_i, the error is $\mathcal{O}(h^k)$ where $k \geq 1$ is dependent on the integration scheme used and h is the separation between adjacent points.

Let us compare the error scaling between these two methods more closely. Suppose that we are integrating f over a d-dimensional hypercube with side-length L, then $N = (L/h)^d$ implies $h^k = LN^{-k/d}$. So, we see that quadrature has an error scaling $\propto N^{-k/d}$ while the error of the Monte Carlo estimator always scales as $\propto N^{-1/2}$, independent of dimension. Therefore, as long as the dimensionality of the space is high enough such that $d > 2k$, Monte Carlo integration is more favorable in terms of computational efficiency. This makes Monte Carlo methods the preferred choice when tackling integrals over very high dimensional spaces.

2.2.2 Markov Chain Monte Carlo

We want to formulate our problem of computing high-dimensional configuration-space integrals such that it is amenable to Monte Carlo methods. However, directly adopting the scheme described in the previous section does not quite work. Typically, the significant contributions come from small regions in the integration domain while being negligible outside. Therefore, the bulk of the uniformly sampled points fall outside of these significant regions where the integrand vanishes, leading to large statistical errors. If we knew the locations of these significant regions, then we could modify our sampling distribution to favor sampling points from these regions, a technique called *importance sampling*. Unfortunately, we typically do not know a priori where the significant regions are.

There is however an elegant solution, which is to implement importance sampling through means of a guided random walk in configuration space that preferentially visits regions of importance. To do this, the guided random walk is represented as a *Markov chain*, which is a sequence of configurations $\{X_i\}_{i=1}^{N}$ such that the probability of the sequence is

$$P(X_1, X_2, ..., X_N) = P(X_1)T(X_1 \to X_2)\cdots T(X_{N-1} \to X_N) \tag{2.24}$$

where $T(X \to X')$ is a matrix containing the transition probabilities between each pair of states and $P(X_1)$ is the probability of having the initial configuration X_1, which we set to 1 for simplicity. In other words, the probability of sampling the next configuration X' only depends on the last state X through $T(X \to X')$, oblivious to the full history of the chain. Thus, Markov chains are said to be *memoryless*.

Remarkably, as long as the Markov chain is *aperiodic* and *connected*, then in the limit that $N \to \infty$, the sampled configurations will approach those sampled from some unique probability distribution $P(X)$, termed the *stationary distribution*. To further elaborate, aperiodic means that the probability of the chain revisiting a configuration after n steps is non-zero for all n, while connectedness means that every configuration is reachable from every other configuration within a finite number of steps. Together, these two properties imply the chain is *ergodic*, loosely meaning that the chain visits all possible configurations given a sufficient amount of time. Intuitively, if the Markov chain can explore any other possible configuration in statistically the same way no matter where it starts from, then the chain always “forgets” the initial configuration in the long run due the memoryless property. The situation is analogous to a system reaching thermal equilibrium in statistical mechanics, at which point all information about the initially prepared state is erased (except for conserved quantities), and the system can be described by a universal (Boltzmann) probability distribution.

Our goal is to tune the transition matrix $T(X \to X')$ such that the chain converges to a stationary distribution equal to $\pi(\mathbf{X})$ given by Eq. (2.9), so that we can approximate thermal expectation values as statistical averages over generated configurations from the chain. To find out what form $T(X \to X')$ needs to take, a useful result is first introduced. Denote the state index as t and $P(X,t)$ as the probability of having $X_t = X$ in the chain $\{X_i\}_{i=1}^{N}$ for $1 \leq t \leq N$. Then

$$P(X,t+1) = \sum_{X'} T(X' \to X)P(X',t) \tag{2.25}$$

is the *Chapman-Kolmogorov equation.* The stationarity condition thus implies that there exists a probability distribution $P(X)$ such that $P(X) \equiv P(X,t) = P(X,t+1)$ as the probability distribution is unchanging. We have then that

$$\sum_{X'} T(X' \to X)P(X') = \sum_{X'} T(X \to X')P(X) \tag{2.26}$$

which essentially states that the flux of probability into and out of X must balance each other for steady-state invariance of $P(X)$. For a given choice of $T(X \to X')$, the stationary distribution $P(X)$ is dictated such that the probability conservation law is fulfilled. Let us postulate that $T(X \to X')$ and $P(X)$ satisfy a even stronger condition at equilibrium

$$T(X' \to X)P(X') = T(X \to X')P(X) \tag{2.27}$$

for all pairs $X, X' \in S$. This condition is known as *detailed balance*, stating that the probability flows between each pairs of states X, X' cancel each other out. It is obvious that this condition implies the previous 'global' conservation law. Hence, as long as $T(X \to X')$ satisfies detailed balance involving $P(X)$, the chain will converge to $P(X)$ as its stationary distribution.

For the Monte Carlo calculations in this thesis, we use the **Metropolis algorithm**, which corresponds with writing the transition probability $T(X \to X')$ as the product of a *proposal probability* $G(X \to X')$ and *acceptance probability* $A(X \to X')$

$$\begin{aligned} T(X \to X') &= G(X \to X')A(X \to X') \\ A(X \to X') &= \min\left(1,\ \frac{G(X' \to X)P(X')}{G(X \to X')P(X)}\right) \end{aligned} \tag{2.28}$$

Let us prove that this satisfies Eq. (2.27). First, assume $G(X' \to X)P(X') < G(X \to X')P(X)$, so that $A(X \to X') = \frac{G(X' \to X)P(X')}{G(X \to X')P(X)}$ and $A(X' \to X) = 1$. We then have $T(X \to X')P(X) = G(X' \to X)P(X')$. However, we also have $T(X' \to X)P(X') = G(X' \to X)P(X')$, and so Eq. (2.27) holds for this case. The remaining case $G(X' \to X)P(X') \geq G(X \to X')P(X)$ follows from identical reasoning, and so, we have proven that the Metropolis algorithm satisfies detailed balance. ■

To perform the procedure, an initial configuration X_1 is chosen. Then, the chain is built up through the following process. Given the current state X, a trial state X' is first drawn from the proposal distribution $G(X \to X')$ and accepted with probability given by $A(X \to X')$. In practice, the acceptance stage is implemented through generating a uniform random number u on $[0, 1]$. If $u < A(X \to X')$, then the next element of the chain is set to be trial state X'. Otherwise, the trial state is rejected and the next state of the chain is set to be the previous state X. After a burn-in (thermalization) period, the initial data X_1 will be essentially erased and the chain will have converged to the desired stationary distribution, sampling configurations according to it.

Again, for our problem of computing thermal expectation values, the configuration space is the space of world line configurations $\{\mathbf{X}\}$ and the stationary distribution is set to be $\pi(\mathbf{X})$ from Eq. (2.9). After the chain's equilibration, the generated samples $\{\mathbf{X}_i\}_{i=1}^{P}$ can be used for approximating physical quantities as simple averages

$$\left\langle \hat{O} \right\rangle \approx \frac{1}{P} \sum_{i=1}^{P} w(\mathbf{X}_P) \tag{2.29}$$

It remains to specify the form of the proposal probability $G(X \to X')$, which should chosen judiciously for the algorithm to run efficiently.

2.2.3 Sampling of Elementary Moves

The way that imaginary-time paths are updated during the procedure is crucial - we must design our proposal distribution $G(X \to X')$ in such a way that ensures effective exploration of the configuration space during the Metropolis random walk. In general, it means that moves involving multiple beads are necessary as just moving a single bead turns out to be too inefficient.

A commonly-used move in path integral Monte Carlo for efficient sampling is the *wiggle* move. The update consists of choosing a single world line from the configuration, and selecting a segment of that world line. The world line is then chopped off at the end points of that segment, and a new segment joining the two end points is then proposed as a modification to the existing world line and accepted using the Metropolis recipe (2.28). The positions of the beads along the proposed new segment can conveniently be drawn from Gaussian probability distributions centered at the corresponding beads in the old segment, since the short-time propagators $\rho(\mathbf{R}, \mathbf{R}'; \epsilon)$ in the Eq. (2.9) distribution have the free propagator ρ_F as a factor, which is a Gaussian from Eq. (2.14).

For sake of computational efficiency, the Metropolis proposal and acceptance stages for the wiggle move can be combined into one sequential, multi-level procedure [35–37], in which first (at the zero-th level) the midpoint position of the new segment is generated and then accepted or rejected according to some acceptance probability. If accepted, the procedure moves on to the next level, where new midpoint positions are generated for each of the sub-segments demarcated by the midpoint position from the previous level, moving on to the next level if the new positions are accepted. This process of bisection continues until all positions in the new segment have been generated. If at any level the proposed midpoint positions are rejected, then the entire move is aborted and the old world line is retained.

The wiggle move contains a parameter s which is the length of the segment that

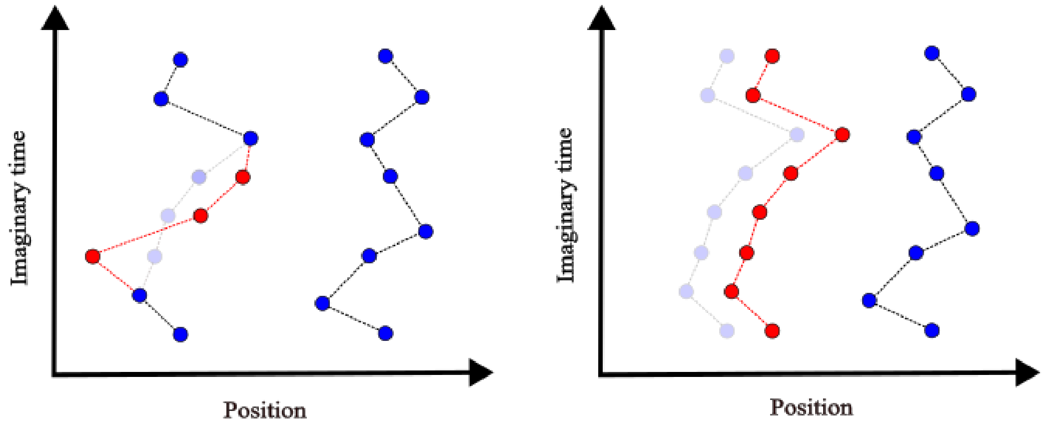

Figure 2.3: *Left:* Wiggle move involving three beads applied to a particle world line. The segment in red shows the proposed world line modification. *Right:* Displace move applied to a particle world line.

is being updated. If s is made too large, it becomes very likely that the move will be rejected and nothing gets done. Conversely, if s is too small, the resulting move will be too insignificant. As can be seen, both making s too big or too small results in inefficient exploration. Therefore, the value of s has to be tuned throughout the simulation to maintain the acceptance rate of moves within a permissible range, which for example can be taken to be from 20% to 50% [36].

In addition to the wiggle move, *displace*-type moves involving rigid displacements of world lines can also be incorporated into the sampling algorithm to improve overall exploration of the configuration space. The magnitude Δ of the displacement also ought to be tuned to maintain desired acceptance rates. For the PIGS variant of path integral Monte Carlo we will see in Section 2.4.1, the world lines are open, and so the wiggle move can also involve the ends of the world lines, now termed the *wag* move. When multiple types of moves are available, one of them is randomly chosen to be performed during each step of the simulation. Depictions of the wiggle and displace updates are shown in Fig. 2.3.

Altogether, the scheme we have discussed thus far using Monte Carlo to evaluate thermal expectation values (2.2) is known as 'conventional' path integral Monte Carlo.

As we will see in the next section, we begin running into scalability issues when trying to incorporate quantum statistics into the methodology.

2.3 Effects of Particle Indistinguishability

So far in our discussion, we have treated all particles as distinguishable. That is, we have ascribed particle 1 with position $\mathbf{r}_1$, particle 2 with position $\mathbf{r}_2$, and so on. However, it is an empirical fact that particles with the same quantum numbers are indistinguishable; no experiment can tell you otherwise. We cannot say that atom i is at a particular position, only that an atom is at that particular position. The same goes for any other quantum number, therefore the labelling of any atom in the system is redundant. The effects of indistinguishability for systems of quantum particles leads to observable consequences, notably the Pauli Exclusion Principle for fermions and conversely an effective attraction between bosons as in Bose-Einstein condensation.

To incorporate the concept of particle indistinguishability, we postulate that that the system's Hamiltonian (describing N identical particles) always possesses particle permutation symmetry. Since any permutation is the composition of transpositions, let us define a transposition operator $\hat{P}_{\alpha\beta}$ on the system's Hilbert space, whose action is to swap the labels on particles α and β. It can readily be seen that $\hat{P}^2_{\alpha\beta} = 1$, meaning that the eigenvalues of $\hat{P}_{\alpha\beta}$ must have magnitude 1. While it is possible in some physical scenarios to consider the possibility of complex eigenvalues $e^{i\theta}$, such as for anyonic statistics, they are irrelevant to the current discussion, where we will restrict ourselves to $\eta = \pm 1$ as the permissible eigenvalues of $\hat{P}_{\alpha\beta}$. The eigenstates of $\hat{P}_{\alpha\beta}$ are then given by

$$\hat{P}_{\alpha\beta}\phi(\mathbf{r}_1, ..., \mathbf{r}_\alpha, ..., \mathbf{r}_\beta, ..., \mathbf{r}_N) = \eta\phi(\mathbf{r}_1, ..., \mathbf{r}_\alpha, ..., \mathbf{r}_\beta, ..., \mathbf{r}_N) \tag{2.30}$$

The spin-statistics theorem provides the connection between η and the spin angular momenta of the particle species involved. For bosons, which have integer spin, $\eta = 1$, and for fermions, which have half-integer spin, $\eta = -1$. Since we also have by definition that

$$\hat{P}_{\alpha\beta}\phi(\mathbf{r}_1, ..., \mathbf{r}_\alpha, ..., \mathbf{r}_\beta, ..., \mathbf{r}_N) = \phi(\mathbf{r}_1, ..., \mathbf{r}_\beta, ..., \mathbf{r}_\alpha, ..., \mathbf{r}_N) \tag{2.31}$$

the eigenstates of $\hat{P}_{\alpha\beta}$ acquire a factor of η whenever two particles are swapped, and are said to be (anti-)symmetric with respect to particle exchange. Mathematically, permutation symmetry is implemented by having $[\hat{H}, \hat{P}_{\alpha\beta}] = 0$, and so $\hat{H}$ and $\hat{P}_{\alpha\beta}$ have a shared eigenbasis. Additionally, η must be a conserved quantity and the system's time evolution is restricted to a subspace spanned by either symmetric (or antisymmetric) energy eigenstates depending on whether the system is composed of bosons or fermions. This means that only states of the appropriate symmetry contribute to the propagator.

To simplify the notation, let us write $\mathbf{R} = \mathbf{r}_1 \cdots \mathbf{r}_N$. We can define an operator $\hat{S}_\eta$ that projects states onto the correct symmetry subspace, which we call the *symmetrizer*, defined through its action on a wavefunction $\psi(\mathbf{R})$

$$\hat{S}_\eta \phi(\mathbf{R}) = \frac{1}{N!} \sum_P \eta^P \psi(P\mathbf{R}) \tag{2.32}$$

where P is a permutation of the particle labels, $\eta = \pm 1$ for bosons and fermions respectively, and $\eta^P = (\text{sgn}(P))^{(1-\eta)/2}$. Note that the propagator has an expansion in terms of Hamiltonian eigenstates $\{\phi_j\}$:

$$\rho(\mathbf{R}, \mathbf{R}'; \beta) = \sum_{j=0}^{\infty} \phi_j^*(\mathbf{R})\phi_j(\mathbf{R}')e^{-\beta E_j} \tag{2.33}$$

By applying the bosonic ($\eta = 1$) symmetrizer to the propagator, we see that it projects out states of appropriate symmetry

$$\begin{aligned}\hat{S}_{\eta=1}\rho(\mathbf{R}, \mathbf{R}'; \beta) &= \frac{1}{N!} \sum_{j=0}^{\infty} \sum_P \phi_j^*(P\mathbf{R})\phi_j(\mathbf{R}')e^{-\beta E_j} \\ &= \frac{1}{N!} \left(\sum_{P,\,\text{even}} + \sum_{P,\,\text{odd}} \right) \left(\sum_{\text{Bose, j}} + \sum_{\text{Fermi, j}} \right) \phi_j^*(P\mathbf{R})\phi_j(\mathbf{R}')e^{-\beta E_j} \\ &= \sum_{\text{Bose}} \phi_j^*(\mathbf{R})\phi_j(\mathbf{R}')e^{-\beta E_j}\end{aligned} \tag{2.34}$$

where in the second equality we split the permutation sum $\sum_P$ into sums $\sum_{P,\text{even}}$, $\sum_{P,\text{odd}}$ over even and odd parity permutations, as well as split the sum over Hamiltonian eigenstates $\sum_{j=0}^{\infty}$ into sums $\sum_{\text{Fermi, j}}$, $\sum_{\text{Bose, j}}$ over (anti-)symmetric Hamiltonian eigenstates. Applying the symmetrizer to $\mathbf{R}'$ instead yields the same result. An analogous calculation can be performed with the fermionic symmetrizer to show that it projects out antisymmetric, fermionic states. When a permutation is applied to an argument of the symmetrized propagator $\hat{S}_\eta \rho$, we obtain

$$(\hat{S}_\eta \rho)(P\mathbf{R}, \mathbf{R}'; \beta) = \eta^P (\hat{S}_\eta \rho)(\mathbf{R}, \mathbf{R}'; \beta) \tag{2.35}$$

With this result, replacing all propagators with their symmetrized versions in the expectation value gives

$$\left\langle \hat{O} \right\rangle = \frac{\sum_P \eta^P \left\langle \hat{O} \right\rangle_P}{\sum_P \eta^P} \tag{2.36}$$

where $\left\langle \hat{O} \right\rangle_P$ denotes the expectation value of $\hat{O}$ for configurations $\mathbf{X}$ closing on a permutation P of the starting positions: $\mathbf{R}_M = P\mathbf{R}_0$.

The importance of considering particle indistinguishability depends on the degree that the single particle wavefunctions overlap. The extent of a particle's spatial delocalization at a given temperature T is roughly quantifiable by the thermal de Broglie wavelength

$$\lambda_T = \frac{h}{\sqrt{2\pi m T}} \tag{2.37}$$

When the interparticle spacing is much greater than the thermal de-Broglie wavelength, the identity permutation dominates in Eq. (2.36). In the limit of zero temperature, the thermal wavelength diverges and all $N!$ permutations become equally important. Unfortunately, for fermionic systems this leads to the infamous *sign problem*, making it intractable for Monte Carlo methods to handle large systems of identical fermions. The heart of issue can be summarized as the expectation value becoming a summation over terms of alternating sign that cancel each other out almost exactly, leading to the calculation becoming overwhelmed by the statistical noise intrinsic to Monte Carlo methods.

For bosonic systems however, this is no issue since the terms do not change sign depending on the permutation's parity. We simply have adapt our sampling procedure to also sample permutations of particles throughout the duration of the simulation. In other words, the random walk is now over both the space of world-line configurations and space of permutations. Schemes for sampling permutations are described in Refs. [35, 36]. The way that they work is that an additional 'permute' move is added to the sampling repertoire. In its most basic incarnation, the permute move involves choosing a particular time slice of $\mathbf{X}$ and disconnecting the links connecting that slice to the previous time slice, then reconnecting the beads differently, as depicted in Fig. 2.4 for a simple case. The more general scheme has no restriction that the reconnection of paths must take place within a single time slice [36]. When two world lines are involved in a permutation, they become intertwined with each other and are said to form a *permutation* or *exchange* cycle. The indistinguishability of particles correlates with the appearance of exchange cycles involving macroscopically many world lines. It turns out that these macroscopic exchange cycles are what underlie

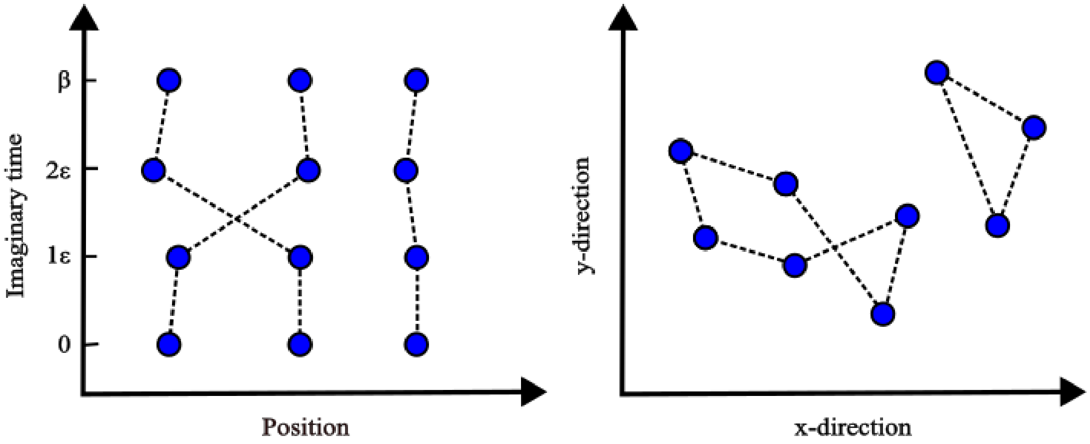

Figure 2.4: *Left:* A permutation is applied to the $t = 2\epsilon$ time slice of the configuration $\mathbf{X}$ containing $N = 3$ particle world lines. *Right:* As a result of the permutation, two of the world lines become entangled, while the remaining one is left unchanged since it is not involved in the permutation.

phenomena such as superfluidity and Bose-Einstein condensation.

Conventional PIMC starts running into problems when attempting to sample large exchange cycles. For a particle world line, if we imagine the links as carrying a 'portion' of a particle as well, rather than just the beads, then the permutation brings the two particles closer together, even though the bead positions are unchanged. Essentially all interactions between particles found in nature contain some sort of strong repulsion at short distances. Thus, bringing two particles too close together will spike the system's potential energy, leading to a high probability of rejection of the move. This has the effect of exponentially suppressing exchanges involving higher numbers of particles, which is problematic for witnessing superfluidity in our simulations.

The continuous-space Worm Algorithm [38] was developed in large part for efficient sampling of permutations, operating within an extended configuration space containing the subspace of closed world line configurations (called the Z-sector, which is sampled from in conventional PIMC) as well as configurations containing a single open world line (called the G-sector). The inclusion of G-sector configurations allows for permutation cycles to be sampled without having to bring particles close together and incurring the cost of potential energy. The resulting performance boost was applied to great effect in Ref. [38], where the superfluid transition of helium-4 was simulated for thousands of atoms, while the previously largest system size simulated contained sixty-four atoms [39]. Since the details of the algorithm are lengthy, we will not delve into them in this thesis and instead kindly refer the reader to Refs. [38, 40]. The Worm Algorithm's formulation also lends itself naturally to simulating in the grand canonical ensemble, where the particle number can fluctuate. In Chapter 3 however, a canonical variant of the algorithm is utilized in which the particle number is fixed for simulations of a helium-4 monolayer over graphene.

2.4 Zero temperature methods

Suppose one is interested in zero temperature, for example, in order to study the system's ground state properties. At exactly $T = 0$ K, the imaginary time path lengths β diverge to infinity, rendering it impossible to utilize the formalism described above. One way to get around this is to take T as low as possible such that the obtained estimates can effectively be treated as ground state estimates. However, there also exists a specialized set of 'zero-temperature' methods aimed specifically at describing $T = 0$ K. Although they may not be as flexible as finite temperature approaches, one could argue that they have comparable or even better efficiency when it comes to specifically extracting the ground state properties.

We shall discuss two methods in particular: Diffusion Monte Carlo (DMC) and Path Integral Ground State (PIGS) (also referred to as the Variational Path Integral method in the literature). Instead of starting from the thermal density matrix (2.1), these methods consider the many-body Schrödinger equation in imaginary time

$$\frac{\partial \Psi(\mathbf{R},t)}{\partial t} = \mathcal{H}(\mathbf{R})\Psi(\mathbf{R},t) = \left(-\lambda \sum_i \nabla_i^2 + V(\mathbf{R})\right)\Psi(\mathbf{R},t) \tag{2.38}$$

where $\lambda \equiv \hbar^2/2m$ as before. In imaginary time, the Schrödinger equation becomes a diffusion equation. By expanding in the eigenbasis $\{\phi_j\}$ of the Hamiltonian $\mathcal{H}$, this equation can be readily solved in order to yield

$$\Psi(\mathbf{R},t) = \sum_{j=0}^{\infty} c_j e^{-E_m t}\phi_j(\mathbf{R}) = e^{-E_0 t}\left[c_0\phi_0(\mathbf{R}) + \sum_{j=1}^{\infty} c_j e^{-(E_j - E_0)t}\phi_j(\mathbf{R})\right] \tag{2.39}$$

Therefore in the long time limit, the excited state contributions die out and the true ground state is 'projected out' up to some constant factor, provided that there is non-zero overlap $c_0 \neq 0$ between the ground state wavefunction and $\Psi(\mathbf{R},0)$.

As seen from Eq. (2.39), the contribution from the first excited state persists the longest throughout the projection procedure, the decay rate of which is given by the energy gap $\Delta E = E_1 - E_0$ between the ground and first excited state. For bosonic systems, the ground state wavefunction is positive everywhere, hence any wavefunction $\Psi(\mathbf{R}, 0)$ that is also positive everywhere will suffice as it is guaranteed to have non-zero overlap. For fermionic systems however the story is different, as the ground state wavefunction is *nodal*: there are regions where the ground-state wavefunction flips sign due to the anti-symmetry under permutations[1].

Starting out from some choice of $\Psi(\mathbf{R}, 0)$, the objective of zero-temperature Monte Carlo methods is to then obtain the asymptotic limit $\psi(\mathbf{R}, t \to \infty)$.

2.4.1 Path Integral Ground State (PIGS)

The path integral ground state (PIGS) method functions almost identically to finite-temperature PIMC. The main difference is that as in Eq. (2.38), the imaginary-time paths must now involve an initial trial state $|\psi_0\rangle$ that is propagated in imaginary time

$$|\psi(\Lambda)\rangle = e^{-\Lambda \hat{H}} |\psi_0\rangle \tag{2.40}$$

where $\psi(\mathbf{R}, 0) = \langle \mathbf{R} | \psi_0 \rangle$ gives the trial wavefunction. This is the basis-independent solution to Eq. (2.38), where Λ is a variational parameter called the *projection time*. Note that Λ does not have any connection with temperature, but rather is a artificial parameter that is increased sufficiently for the state given in Eq. (2.40) to converge to the ground state. Expectation values are now given by

$$\left\langle \hat{O} \right\rangle_{\text{PIGS}} = \frac{\langle \psi(\Lambda) | \hat{O} | \psi(\Lambda) \rangle}{\langle \psi(\Lambda) | \psi(\Lambda) \rangle} = \frac{\langle \psi_0 | e^{-\Lambda \hat{H}} \hat{O} e^{-\Lambda \hat{H}} | \psi_0 \rangle}{\langle \psi_0 | e^{-2\Lambda \hat{H}} | \psi_0 \rangle} \tag{2.41}$$

Again, a path integral representation of this equation may be written down by expanding the propagator as the convolution of M short-time propagators. For the denominator, this gives

$$Z(\Lambda) \equiv \langle \psi(\Lambda) | \psi(\Lambda) \rangle = \int \mathrm{d}\mathbf{R}_0 \cdots \mathrm{d}\mathbf{R}_{2M}\, \psi_0(\mathbf{R}_0) \psi_0(\mathbf{R}_{2M}) \prod_{j=0}^{2M-1} \rho(\mathbf{R}_j, \mathbf{R}_{j+1}; \epsilon) \tag{2.42}$$

---

[1] Specialized methods have been developed to work around these nodal regions, delimited from each other by so-called nodal surfaces. One of these methods is the *fixed-node method*, where we forbid the Monte Carlo random walks from crossing nodal surfaces.

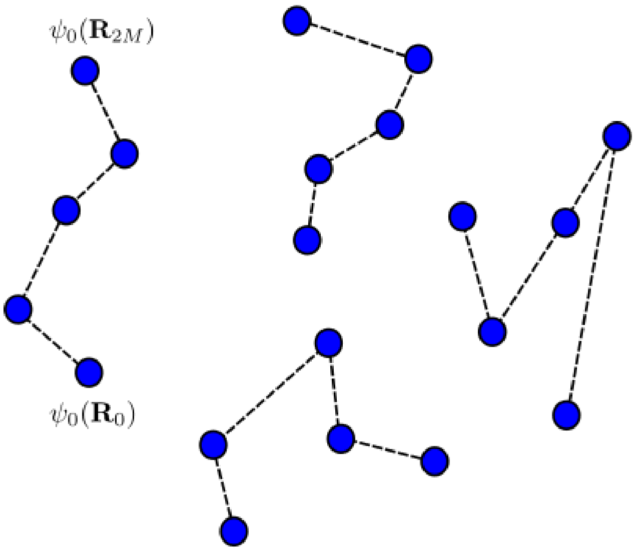

Figure 2.5: A sampled configuration $\mathbf{X}$ during PIGS. The world lines are now all open. When a Monte Carlo update changes the ends, the proposal/acceptance probabilities now involve the trial wavefunction.

where $\Lambda = M\epsilon$. It suggests that the expectation value may again be written as the integration with respect to a probability density, but this time it is given by

$$\pi_{\mathrm{PIGS}}(\mathbf{X}) \propto \psi_0(\mathbf{R}_0)\psi_0(\mathbf{R}_{2M}) \prod_{j=0}^{2M-1} \rho(\mathbf{R}_j, \mathbf{R}_{j+1}; \epsilon) \tag{2.43}$$

where again, we simplify the notation by denoting $\mathbf{X} = \mathbf{R}_0 \cdots \mathbf{R}_{2M}$, with Eq. (2.42) giving the proper normalization so that we have $\int \mathrm{d}\mathbf{X}\, \pi_{\mathrm{PIGS}}(\mathbf{X}) = 1$.

Comparing with the distribution that is sampled from in finite temperature PIMC, the PIGS distribution now has dependence on a trial wavefunction and is supported over the set of 'open' instead of 'closed' world line configurations, since the trace is no longer involved. An example world line configuration in PIGS is depicted in Fig. 2.5. Analogously to the finite temperature case described earlier, we have that

$$\left\langle \hat{O} \right\rangle_{\mathrm{PIGS}} = \int \mathrm{d}\mathbf{X}\, \pi_{\mathrm{PIGS}}(\mathbf{X}) w(\mathbf{X}) \tag{2.44}$$

for a suitable weight function $w(\mathbf{X})$ associated with the observable $\hat{O}$. In the limit of $\Lambda \to \infty$, the midpoint configurations obtained approach that from sampling a probability density proportional to $|\phi_0|^2$, irrespective of the trial wavefunction that was used.

As an illustrative example of computing a physical observable through PIGS, we can use the position representation of the Hamiltonian $\langle \mathbf{R}| \hat{H} |\mathbf{R}'\rangle = \delta(\mathbf{R}-\mathbf{R}')\mathcal{H}(\mathbf{R}')$ to derive a path integral representation for the total energy:

$$
\begin{aligned}
E = \left\langle \hat{H} \right\rangle &= Z(\Lambda)^{-1} \int \mathrm{d}\mathbf{R}\, \mathrm{d}\mathbf{R}'\, \psi_0(\mathbf{R})\psi_0(\mathbf{R}')\rho(\mathbf{R},\mathbf{R}';2\beta) \frac{\mathcal{H}\psi_0(\mathbf{R}')}{\psi_0(\mathbf{R}')} \\
&= \int \mathrm{d}\mathbf{X}\, \pi_{\mathrm{PIGS}}(\mathbf{X}) \left\{ \frac{\mathcal{H}\psi_0(\mathbf{R}_M)}{\psi_0(\mathbf{R}_M)} \right\}
\end{aligned}
\tag{2.45}
$$

The weight function corresponding to this case is $w(\mathbf{X}) = \frac{\mathcal{H}(\mathbf{R}_M)\psi_0(\mathbf{R}_M)}{\psi_0(\mathbf{R}_M)}$, which is termed the *local energy.* Note that in Eq. (2.45) the trial wavefunction is evaluated at the middle time slice of configuration $\mathbf{X}$, although in principle any other time slice can be taken because the Hamiltonian commutes with the evolution operator.

Eq. (2.45) gives rise to the so-called *mixed estimator* for convenient calculations of the total energy. If we have a set of paths $\{\mathbf{X}_j\}_{j=1}^{P}$ distributed according to $\pi(\mathbf{X})$, such as those from the Monte Carlo sampling procedure described in Section 2.2, E can be approximated as

$$
E \approx \frac{1}{P} \sum_{j=1}^{P} \frac{\mathcal{H}(\mathbf{R}_M^{(j)})\psi_0(\mathbf{R}_M^{(j)})}{\psi_0(\mathbf{R}_M^{(j)})}
\tag{2.46}
$$

which can be evaluated quite efficiently given the analytical expression for $\psi_0(\mathbf{R})$. At this point it may be asked: what about quantum statistics? Doesn't it necessitate the sampling of permutations? Fortunately, the situation here is a lot simpler than the finite-temperature case. Since the ground state wavefunction for a system of distinguishable particles is the same as for a system of identical bosons, it turns out not to be necessary to sample permutations.

2.4.2 Diffusion Monte Carlo (DMC)

The diffusion Monte Carlo method implements importance sampling of Eq. (2.38) through rewriting its solution as $f(\mathbf{R},t) = \psi_G(\mathbf{R})\Psi(\mathbf{R},t)$ where $\psi_G(\mathbf{R})$ is a *guide* *wavefunction*. When substituted, Eq. (2.38) becomes

$$\begin{aligned} -\frac{\partial f(\mathbf{R},t)}{\partial t} &= D_{\mathbf{R}} f(\mathbf{R},t) \\ D_{\mathbf{R}} &\equiv -\lambda \sum_{i=1}^{N} \nabla_i^2 - 2\lambda \nabla \cdot \frac{\nabla \psi_G(\mathbf{R})}{\psi_G(\mathbf{R})} + (E_L(\mathbf{R}) - E_T) \end{aligned} \tag{2.47}$$

where we have added a constant energy shift E_T to the Hamiltonian which is methodologically important, $\lambda = \hbar^2/2m$ is the diffusion constant, and $E_L(\mathbf{R}) = \mathcal{H}\psi_G/\psi_G$ is the local energy of the guide wavefunction.

The three terms in (2.47) are referred to as the *diffusion*, *drift*, and *branching* terms respectively. Retaining only the first term, the situation would be quite boring: $f(\mathbf{R},t)$ would only diffuse spatially outwards in order to minimize the kinetic energy. Adding the second term provides the 'quantum force'

$$F(\mathbf{R}) = 2\nabla \cdot \frac{\nabla \psi_G(\mathbf{R})}{\psi_G(\mathbf{R})} \tag{2.48}$$

acting to guide this diffusion process towards regions where $\psi_G(\mathbf{R})$ is large. The third term is involved in a branching and pruning step of the DMC algorithm.

To solve Eq. (2.47), we use a Green's function approach. The imaginary-time evolution of f over the course of a small time step Δt in accord with Eq. (2.47) comes from convolving with the Green's function $G(\mathbf{R},\mathbf{R}';\Delta t)$, which is the unique solution with the initial condition $G(\mathbf{R},\mathbf{R}';0) = \delta(\mathbf{R}-\mathbf{R}')$

$$\begin{aligned} G(\mathbf{R},\mathbf{R}';t) &= \langle \mathbf{R}| \, e^{-tD_{\mathbf{R}}} \, |\mathbf{R}'\rangle \\ f(\mathbf{R},t+\Delta t) &= \int \mathrm{d}\mathbf{R}' \, G(\mathbf{R},\mathbf{R}';\Delta t) f(\mathbf{R}',t) \end{aligned} \tag{2.49}$$

Similar to the path integral case, we proceed by substituting a short-time approximation for the Green's function

$$G(\mathbf{R},\mathbf{R}';\Delta t) = \frac{e^{-(\mathbf{R}-\mathbf{R}'-\lambda\Delta t F(\mathbf{R}'))^2/4\lambda\Delta t - \Delta t\left(\frac{E_L(\mathbf{R})+E_L(\mathbf{R}')}{2} - E_T\right)}}{(4\pi\lambda\Delta t)^{3N/2}} + \mathcal{O}(\Delta t^2) \tag{2.50}$$

Then, $f(\mathbf{R}, t \to \infty)$ is found by repeatedly iterating Eqs. (2.49) and (2.50).

In order to implement this procedure, the distribution $f(\mathbf{R},t)$ is represented through a population of n walkers that each perform independent random walks, each walker constituting a pair $(\mathbf{R}_i, w_i)$ where $\mathbf{R}_i$ is the $3N$-dimensional position vector of all particles and w_i is the walker's weight. To begin, the guide wavefunction $\psi_G(\mathbf{R})$ as well as the initial distribution $f(\mathbf{R}, 0)$ have to be chosen, with $\psi_G(\mathbf{R})$ approximating the true ground state as closely as possible. One often starts from an ansatz and variationally minimizes its expected energy in order to obtain a suitable $\psi_G(\mathbf{R})$. Afterwards, $f(\mathbf{R}, 0)$ can be taken to be $|\psi_G(\mathbf{R}, t)|^2$ and the positions of the walkers are initialized according to a probability density proportional to $f(\mathbf{R}, 0)$.

A step during the DMC algorithm consists iterating over all walkers and proposing new positions according to the diffusive kernel given in Eq. (2.50). That is, for a given walker j, it is shifted to a new position $\mathbf{R}'_j = \mathbf{R}_j + \lambda \Delta t F(\mathbf{R}) + \eta$ where η is a $3N$-dimensional Gaussian random vector with mean 0 and variance $2\lambda\Delta t$ for all entries, and the move is then accepted with the Metropolis update probability

$$A(\mathbf{R} \to \mathbf{R}', t) = \min\left(1, \frac{|\psi_G(\mathbf{R}')|^2 G(\mathbf{R}', \mathbf{R}; \Delta t)}{|\psi_G(\mathbf{R})|^2 G(\mathbf{R}, \mathbf{R}'; \Delta t)}\right) \tag{2.51}$$

After moves have been attempted for all walkers, the simulation time is advanced by Δt. The other factor in the Green's function is called the branching factor, given by

$$B_j = \exp\left[-\Delta t\left(\frac{E_L(\mathbf{R}_j) + E_L(\mathbf{R}'_j)}{2} - E_T\right)\right] \tag{2.52}$$

and can be incorporated into the algorithm by multiplying it into the weight of each walker that was moved. However, this turns out to be very inefficient as some walkers will accumulate small weights and have relatively small influence over the final result, yet incur the same computational cost as the important walkers. Therefore, it proves convenient to reconfigure the walkers now and then over the course of the simulation through a *branching and pruning* procedure. To do this, instead of multiplying the branching factor into the walker weights, we determine the *multiplicity* of walker j as $\bar{B}_j = \text{floor}(B_j + \xi)$ where ξ is a uniform random number on $(0, 1)$. If $\bar{B}_j > 0$, $\bar{B}_j - 1$ new copies of walker j are made and addded to the population. Otherwise, walker j is removed.

There is one more ingredient in the algorithm, which is the energy shift E_T that was introduced earlier: it plays the role of keeping the population size stable. As can be seen in Eq. (2.52), the size of the 'average' local energy relative to E_T determines whether the walker should be replicated or removed, corresponding with the overall growth or decay of the population size. Thus, E_T is generally tuned throughout the simulation in order to maintain a population size around a desired walker number n_{target}. As per Ref. [34], one choice is to use

$$E_T = E_{\text{ref}} + C \ln \left(\frac{n_{\text{target}}}{n} \right) \tag{2.53}$$

where E_{ref} is a reference energy that ought to be close to the true ground state energy, n is the current number of walkers, and c is an external parameter.

Altogether, the DMC procedure consists of iterating the diffusion and branching/pruning steps until a target time is reached, corresponding to the asymptotic limit $t \to \infty$. Ideally, by that point the population of walkers represents the true ground state wavefunction, and the walker data $(\mathbf{R}_i, w_i)$ can then be used to compute physical quantities as weighted averages.

Although the DMC method has been applied to obtain ground state estimates for a variety of systems, there are also systematic issues present, notably a bias from having a finite population of walkers [41, 42], as well as a heavy reliance upon the guide wavefunction being a good approximation of the ground state. PIGS on the other hand, does not suffer from this bias as there is no notion of a population. It could be argued that the success of PIGS also heavily depends on the inputted trial wavefunction, which we put to the test in Chapter 3.

2.5 Physical Observables

We have seen how to calculate thermal expectation values through a stochastic algorithm based on Feynman's path integral approach to quantum mechanics. We will now derive the Monte Carlo estimators for a few important physical quantities which we put to use in Chapter 3.

2.5.1 Energy

Let us begin with deriving an estimator for the energy. Eq. (2.9) states that the thermal expectation of any observable $\hat{O}$ (which is a function of the position and momenta of the particles) can be calculated through integration of a suitable weight function $w(\mathbf{X})$ against a probability distribution $\pi(\mathbf{X})$ over the space of all paths $\mathbf{X}$. If $\hat{O}$ is structural, we can simply replace $\hat{\mathbf{R}} \rightarrow \mathbf{R}$ for some time slice $\mathbf{R}$ so that $\hat{O} \rightarrow O(\mathbf{R})$ and use it as our weight function.

The kinetic energy in the Hamiltonian is the only off-diagonal term, and so it is instructive to derive it. For simplicity, we will use the primitive approximation for the propagator. The estimator then follows by computing the action of the kinetic term on the propagator

$$\begin{aligned} \nabla_i \rho(\mathbf{R}, \mathbf{R}'; \epsilon) &= -\frac{(\mathbf{r}_i - \mathbf{r}_i')}{2\lambda\epsilon} \rho(\mathbf{R}, \mathbf{R}'; \epsilon) \\ -\lambda \sum_i \nabla_i^2 \rho(\mathbf{R}, \mathbf{R}'; \epsilon) &= \left(\frac{3N}{2\epsilon} - \frac{(\mathbf{R} - \mathbf{R}')^2}{4\lambda\epsilon^2} \right) \rho(\mathbf{R}, \mathbf{R}'; \epsilon) \end{aligned} \tag{2.54}$$

which gives back the propagator with a prefactor in front. Substituting this result into Eqs. (2.8) and (2.9), the prefactor gives an estimator for the kinetic energy in the primitive approximation, and so the total energy estimator follows trivially because the potential energy is structural

$$E = \frac{3N}{2\epsilon} - \frac{1}{4\lambda\epsilon^2} \left\langle (\mathbf{R}_j - \mathbf{R}_{j+1}')^2 \right\rangle + \langle V(\mathbf{R}_j) \rangle \tag{2.55}$$

where j can be chosen arbitrarily as either 0,1, ..., or $M-1$. For better statistical convergence during run-time, we can then average over j on the right hand side to obtain an improved estimator. Energy estimators based on better approximations of the short-time propagator can be obtained. For example, an estimator based on a fourth-order approximation is derived in Ref. [43], and is given by

$$\frac{N\hbar}{2\epsilon} - \frac{1}{4\lambda\epsilon^2} \left\langle (\mathbf{r}_j - \mathbf{r}_{j+1})^2 \right\rangle + \frac{\lambda\epsilon^2}{9} \left\langle (\nabla V(\mathbf{R}_{2j}))^2 \right\rangle \tag{2.56}$$

It should be emphasized that off-diagonal observables generally require multiple time slices for the calculation. As we will see, computing the superfluid density makes use of the entire world lines of each particle.

2.5.2 Pair distribution function and structure factor

The pair distribution function and structure factor are indispensable quantities when it comes to studying the spatial structure of classical/quantum fluids, and both are readily accessible from experiment. Depending only on the positions of the particles, they are simple to calculate using Monte Carlo generated configurations. We will now present a brief derivation of their formulas starting from equilibrium statistical mechanics, drawing from [44].

Let us assume we have an N-particle system described by Hamiltonian H in the canonical ensemble. If the Hamiltonian is separable: $H = T + V$ with V dependent on position only, the momentum degrees of freedom may be integrated out from the Boltzmann distribution, giving

$$P(\mathbf{r}_1, \mathbf{r}_2, ..., \mathbf{r}_N) = \frac{e^{-\beta V}}{Z_c}\, \mathrm{d}\mathbf{r}_1 \cdots \mathrm{d}\mathbf{r}_N \tag{2.57}$$

which is the probability of having particle 1 in an infinitesimal volume $\mathrm{d}\mathbf{r}_1$, particle 2 in an infinitesimal volume $\mathrm{d}\mathbf{r}_2$, etc where Z_c is the *configurational integral*

$$Z_c = \int \mathrm{d}\mathbf{r}_1 \cdots \mathrm{d}\mathbf{r}_N\, e^{-\beta V(\mathbf{r}_1, ..., \mathbf{r}_N)} \tag{2.58}$$

From now on we will write $\mathbf{r}^N = \mathbf{r}_1 \cdots \mathbf{r}_N$ and similarly $\mathrm{d}\mathbf{r}^N = \mathrm{d}\mathbf{r}_1 \cdots \mathrm{d}\mathbf{r}_N$. In almost every case, one desires to restrict their focus to the distribution of a subset of $n < N$ particles at positions $\mathbf{r}_1, ..., \mathbf{r}_n$, as this gives more insight into the equilibrium structure of the system. The reduced distribution for n particles comes from marginalizing Eq. (2.57) over the remaining $N - n$ extraneous degrees of freedom, and including a combinatorial prefactor $N!/(N - n)!$ as any n-particle subset of the total N may be chosen. And so, we define

$$\rho_N^{(n)}(\mathbf{r}_1, ..., \mathbf{r}_n) = \frac{N!}{(N-n)!} \frac{1}{Z_c} \int \mathrm{d}\mathbf{r}^{(N-n)}\, e^{-\beta V} \tag{2.59}$$

which is called the n-particle density. Note by including the combinatorial prefactor, the normalization is not 1. Particularly,

$$\int \mathrm{d}\mathbf{r}^n \, \rho_N^{(n)}(\mathbf{r}^n) = \frac{N!}{(N-n)!} \tag{2.60}$$

implying that $\rho_N^{(1)}$ has the interpretation as the particle density at point $\mathbf{r}$. More generally, the n-particle density has dimensions of density to the power n. Therefore, if Eq. (2.59) is divided by the product of n densities, a dimensionless measure can be obtained which is more universally applicable. This motivates the definition of the *n-particle distribution function* as

$$g_N^{(n)}(\mathbf{r}^n) = \frac{\rho_N^{(n)}(\mathbf{r}^n)}{\prod_{i=1}^n \rho_N^{(1)}(\mathbf{r}_i)} \tag{2.61}$$

In the scenario that there are no interactions between particles, the numerator of Eq. (2.59) factorizes into one-body terms and $g_N^{(n)}(\mathbf{r}^n) = 1$ as a result.

With interactions however, while $n = 1$ gives us the particle density, $n = 2$ gives information about the two-body correlations present in the system. For fluids, it is commonly assumed that the system is homogeneous and isotropic, i.e. the systems properties do not depend on the position or orientation of the coordinate axes. With these assumptions, the formulae simplify to $\rho_N^{(1)} = \rho$ and $g(r) = g_N^{(2)}(\mathbf{r}_1, \mathbf{r}_2) = \rho_N^{(2)}(\mathbf{r}_1, \mathbf{r}_2)/\rho^2$ where $r = |\mathbf{r}_1 - \mathbf{r}_2|$ where $g(r)$ is referred to as the *radial distribution function*. To proceed, it is illuminating to write the $n = 1$ and $n = 2$ cases in terms of delta functions. First of all, it can be confirmed that

$$\left\langle \sum_{i=1}^{N} \delta(\mathbf{r} - \mathbf{r}_i) \right\rangle = \frac{N}{C_N} \int \mathrm{d}\mathbf{r}^{N-1} e^{-\beta V} = \rho_N^{(1)}(\mathbf{r}) \tag{2.62}$$

as expected. The $n = 2$ case follows similarly

$$\begin{aligned} \left\langle \sum_{i \neq j} \delta(\mathbf{r} - \mathbf{r}_i) \delta(\mathbf{r}' - \mathbf{r}_j) \right\rangle &= \frac{N(N-1)}{C_N} \int \mathrm{d}\mathbf{r}^{N-2} \exp\left(-\beta U(\mathbf{r}, \mathbf{r}', \mathbf{r}_3, ..., \mathbf{r}_N)\right) \\ &= \rho_N^{(2)}(\mathbf{r}, \mathbf{r}') \end{aligned} \tag{2.63}$$

With this result, the radial distribution function may be written in terms of delta functions:

$$\begin{aligned}\left\langle \frac{1}{N}\sum_{i\neq j}\delta(\mathbf{r}-\mathbf{r}_j+\mathbf{r}_\mathbf{i})\right\rangle &= \left\langle \frac{1}{N}\int \mathrm{d}\mathbf{r}'\sum_{i\neq j}\delta(\mathbf{r}'+\mathbf{r}-\mathbf{r}_j)\delta(\mathbf{r}'-\mathbf{r}_i)\right\rangle \\ &= \frac{1}{N}\int \mathrm{d}\mathbf{r}'\rho_N^{(2)}(\mathbf{r}'+\mathbf{r},\mathbf{r}')\end{aligned} \tag{2.64}$$

For an isotropic and homogeneous system, we therefore have

$$\left\langle \frac{1}{N}\sum_{i\neq j}\delta(\mathbf{r}-\mathbf{r}_j+\mathbf{r}_\mathbf{i})\right\rangle = \rho g(r) \tag{2.65}$$

The interpretation of this expression is that on average, the number of particles lying within a shell $[r, r+\mathrm{d}r]$ around some reference particle $\mathbf{r}_i$ is $4\pi r^2\rho g(r)\,\mathrm{d}r$ as can be seen by integrating both sides over a spherical shell $[r, r+\mathrm{d}r]$ centered at $\mathbf{r}_i$. In fact, this is exactly how we compute the pair correlation function in our Monte Carlo simulations. First, the range of distances we want to examine $[r_{\min}, r_{\max}]$ is divided into several equal sized bins of size dr. For a sampled configuration $\mathbf{X}$, the middle time slice $\mathbf{R}$ is extracted. From $\mathbf{R}$, the distances between each pair of particles is calculated and the corresponding bins are incremented accordingly. After averaging over many different configurations $\{\mathbf{X}\}$, each bin in the histogram is normalized by $4\pi r^2\rho/N$ to obtain $g(r)$.

Importantly, the radial distribution function can be related to the potential energy of the system, provided that it consists of only pairwise interactions: $V(\mathbf{r}^N) = \sum_i\sum_{j>i}V(r_{ij})$. The potential part of the system's internal energy is given by

$$\begin{aligned}E_{\text{pot}} &= \frac{1}{Z_c}\int \mathrm{d}\mathbf{r}^N\,V(\mathbf{r}^n)e^{-\beta V(\mathbf{r}^n)} \\ &= \sum_{j>i}\int \mathrm{d}r_i\,\mathrm{d}r_j\,V(r_{ij})\left(\frac{1}{Z_c}\int \mathrm{d}\mathbf{r}^{(N-2)}\,e^{-\beta V(\mathbf{r}^N)}\right) \\ &= \frac{\rho^2}{2}\int \mathrm{d}\mathbf{r}_1\,\mathrm{d}\mathbf{r}_2\,V(r_{12})g_N^{(2)}(\mathbf{r}_1,\mathbf{r}_2) = \frac{N^2}{2\Omega}\int \mathrm{d}\mathbf{r}\,V(r)g(r)\end{aligned} \tag{2.66}$$

which is called the *energy equation*, and can be used for computing corrections to the total energy due to imposing periodic boundary conditions.

Additionally, the radial distribution function $g(r)$ is connected to the *structure factor* of the system, which relates the diffracted intensities obtained from scattering experiments to the microscopic arrangement of scatterers. The structure factor is given by

$$S(\mathbf{q}) = \Omega^{-1} \left\langle \sum_{i,j} \exp\left(-i\mathbf{q} \cdot (\mathbf{r}_i - \mathbf{r}_j)\right) \right\rangle = \Omega^{-1} \left\langle |n(\mathbf{q})|^2 \right\rangle \tag{2.67}$$

with the particle density and its Fourier dual given by

$$\begin{aligned} n(\mathbf{r}) &\equiv \sum_i \delta(\mathbf{r} - \mathbf{r}_i) \\ n(\mathbf{q}) &\equiv \mathcal{F}[n(\mathbf{r})] = \sum_i e^{-i\mathbf{q}\cdot\mathbf{r}_i} \end{aligned} \tag{2.68}$$

For a perfect crystal, the Fourier transform can be evaluated to give

$$n(\mathbf{q}) = \frac{(2\pi)^3}{\Omega} \sum_{\mathbf{G}} \delta^{(3)}(\mathbf{q} - \mathbf{G}) \tag{2.69}$$

where the sum is over all reciprocal lattice vectors associated with the crystal lattice. In other words, the static structure factor has (Bragg) peaks whenever $\mathbf{q}$ equals some reciprocal lattice vector. Making use of Eq. (2.65), Eq. (2.67) can be written in terms of the radial distribution function for an isotropic and homogeneous system

$$S(\mathbf{q}) = \rho + \rho^2 \int \mathrm{d}\mathbf{r}\, e^{-i\mathbf{q}\cdot\mathbf{r}} g(r) \tag{2.70}$$

from which we see the structure factor is simply the Fourier transform of the radial distribution function. This provides a useful consistency check for calculating the structure factor given access to the radial distribution function, and vice-versa.

2.5.3 Superfluid fraction

In this section, we will introduce the two-fluid model of superfluidity, and show how to calculate the superfluid fraction in the two-fluid model using path integral Monte Carlo. Let us begin by discussing the basic physics behind superfluidity. A major breakthrough in the microscopic theory of superfluid helium-4 was made in the 1940s by Soviet physicist Lev Landau, when he realized that the superflow velocity was connected to the elementary excitation spectrum. We will recapitulate his argument in the following.

The thought experiment begins by considering a fluid with total mass M flowing through a narrow pipe with velocity $\mathbf{v}$ in the lab frame. The system's total energy is then

$$E_{\mathbf{v}} = E_0 + \frac{1}{2}M|\mathbf{v}|^2 \tag{2.71}$$

Dissipation of the fluid's kinetic energy due to coupling with the pipe walls occurs through converting a portion of that kinetic energy into creating an elementary excitation with energy $\epsilon(\mathbf{q})$ and momentum $\mathbf{q}$ in the fluid's rest frame. Indeed, in the fluid's rest frame we have that its energy is

$$E_{\mathbf{v}=0,\mathbf{q}} = E_0 + \epsilon(\mathbf{q}) \tag{2.72}$$

where E_0 is the ground state energy of the fluid. If we want to go back to the lab frame, we can perform a Galilean boost with velocity $-\mathbf{v}$ from the rest frame of the fluid. In the boosted frame after creating an elementary excitation, the energy is then

$$E_{\mathbf{v},\mathbf{q}} = E_0 + \epsilon(\mathbf{q}) + \mathbf{q}\cdot\mathbf{v} + \frac{1}{2}M|\mathbf{v}|^2 \tag{2.73}$$

For the process to dissipate energy, it must be that $\epsilon(\mathbf{q}) + \mathbf{q}\cdot\mathbf{v} < 0$, i.e. the excitation has negative energy in the lab frame. This quantity is minimized when $\mathbf{q}$ and $\mathbf{v}$ are anti-parallel, and so it is necessary that $\epsilon(\mathbf{q}) - qv < 0$ for dissipation to occur. The constraint implies a critical velocity v_c, below which no dissipative excitations can be created:

$$v_c = \min_q \frac{\epsilon(\mathbf{q})}{q} \tag{2.74}$$

which is the *Landau criterion* for superflow. The argument happens to have a nice geometric interpretation. At the minimum, the derivative of $\epsilon(\mathbf{q})/q$ vanishes, implying

$$\frac{\mathrm{d}\epsilon(\mathbf{q})}{\mathrm{d}q} = \frac{\epsilon(\mathbf{q})}{q} \quad (\text{at } q = q^\star) \tag{2.75}$$

---

[1] Additionally, Landau's criterion shows it is necessary to have interactions between particles in order for superfluidity to emerge. For a non-interacting system of bosons, the dispersion is given by $\epsilon(\mathbf{q}) = q^2/2m$, which clearly implies the critical velocity is zero - no superflow can exist.

with $q^\star = \operatorname{argmin}_q \frac{\epsilon(\mathbf{q})}{q}$. In other words, to obtain the critical velocity from the graph of $\epsilon(\mathbf{q})$, we can rotate a horizontal line about the origin counter-clockwise. If the line can rotate a finite amount before it touches the dispersion curve, then the system supports superfluidity with critical velocity given by the line's slope.

In the preceding thought experiment, the superfluid constitutes the undisturbed 'ground state' of the system at $T = 0$. As the temperature is increased or the flow velocity exceeds v_c, quasiparticle excitations appear, which one interprets as 'normal' particles that experience viscous friction. The Tisza two-fluid model coarse-grains this picture, considering the superfluid system as comprising of a superfluid and normal component that mix together, yet do not interact with each other. Denote the total mass density as $\rho = Nm/\Omega$ and the superfluid and normal fraction as ρ_s and ρ_n respectively, then we have

$$\rho = \rho_s + \rho_n \tag{2.76}$$

At $T = 0$ K, the system is completely superfluid: $\rho = \rho_s$, while above the critical temperature T_c the system is completely normal: $\rho = \rho_n$, interpolating between these two states when $0 < T < T_c$.

The defining feature of the superfluid portion of particles is that they are decoupled from the boundary motion, unlike the normal portion. The Galilean transformation between fluid rest and moving frames forms a crucial part of Landau's original argument, and in fact, can be used in conjuction with the Tisza two-fluid picture to derive a superfluid fraction estimator for quantum Monte Carlo simulations as shown in Refs. [45, 46]. However, instead of a pipe, we consider the fluid as being sandwiched between two cylinders of radii R and $R + \epsilon$ with $\epsilon << R$. This setup is the same as applying periodic boundary conditions to the pipe with periodicity $2\pi R$. Since the size of the apparatus is large compared to the microscopic scale, locally the particles do not experience the curvature of the boundaries - they see only two planes on either side that are moving with equal velocity $\mathbf{v} = \omega R$.

Now, let us assume that the two cylinders are driven to rotate with a low angular frequency ω. Above the critical temperature T_c, the fluid is completely normal, and equilibrates with the moving walls of the container, rotating together at the same frequency ω. Suppose that the system is then left in flywheel, i.e. left to freely rotate without external intervention. When the temperature is decreased such that $T < T_c$, the fluid acquires a non-zero superfluid portion that decouples from the boundary motion, reducing the moment of inertia and resulting in an increased frequency $\omega' > \omega$ by angular momentum conservation. This principle is what underlies how experiments with torsional oscillators operate to detect superfluidity.

The distinction between 'low' versus 'high' rotation velocities can be made precise, as there is a simple argument showing that the circulation of superflow is quantized. Let us assume that the fluid particles form a condensate, that there is macroscopic occupation of a single quantum state, forgetting the microscopic details of what the individual particles are doing. The position-space wavefunction of the system can then be written as

$$\Psi(\mathbf{r}) = \langle \mathbf{r} | \Psi \rangle = |\Psi| e^{i\phi(\mathbf{r})} \tag{2.77}$$

where $\mathbf{r}$ runs over the volume of the container and the normalization of the state is such that $|\Psi|^2$ is the number density of particles at location $\mathbf{r}$. The system's momentum is then

$$\begin{aligned} \left\langle \hat{\mathbf{P}} \right\rangle &= -i\hbar \int \mathrm{d}\mathbf{r}\, \Psi^* \nabla \Psi \\ &= -i\hbar \int \mathrm{d}\mathbf{r} |\Psi| \nabla |\Psi| + \hbar \int \mathrm{d}\mathbf{r} |\Psi|^2 \nabla \phi(\mathbf{r}) \\ &= \hbar \int \mathrm{d}\mathbf{r}\, |\Psi|^2 \nabla \phi(\mathbf{r}) \end{aligned} \tag{2.78}$$

where the third equality comes from the fact $\hat{\mathbf{P}}$ is Hermitian and hence its expectation must be real. From Eq. (2.78), we can identify $\mathbf{v}_s = \hbar \nabla \phi(\mathbf{r})/m$ as the velocity field, which is irrotational: $\nabla \times \mathbf{v}_s = 0$. Thus, the superfluid's circulation over a closed loop Γ inside the annulus is then given by

$$C = \oint_\Gamma \mathbf{v}_s \cdot \mathrm{d}\mathbf{r} = \frac{\hbar}{m} \oint_\Gamma \nabla \phi(\mathbf{r}) \cdot \mathrm{d}\mathbf{r} \tag{2.79}$$

Since the wavefunction (2.77) must be single valued, the net change in the phase $\phi(\mathbf{r})$ as it winds around the path Γ must be an integer multiple of 2π. We thus have the *Onsager quantization condition* for the circulation

$$C = 2\pi n\hbar/m \tag{2.80}$$

for integer n. We now have an answer for what 'low' velocity means. If the velocity is not high enough to drive a circulation of size h/m, then the superfluid remains at rest. On the other hand, if velocity is 'high', then Eq. (2.80) suggests that a superfluid can settle into persistent, dissipationless currents when set flowing in circles. If the region enclosed by Γ does not have any holes, then Γ can be continuously contracted to a point without affecting the evaluation of Eq. (2.79), making the circulation vanish, so it is necessary to have obstructions for the superfluid to circulate around. Eq. (2.80) also suggests that the circulation may transition between levels through the production of vortices. Indeed, such 'quantum vortices' have been observed in superfluid helium-4 [47] as well as in superconducting films via scanning SQUID microscopy [48].

Due to the equivalence between the annulus and a pipe with periodic boundary conditions, we are motivated to generalize to a system with N identical particles of mass m within a container taken to be a box of dimensions $\Omega = L_1 \times \cdots \times L_d$ with periodic boundary conditions applied to all sides, in other words, a higher-dimensional torus. The box walls and normal fluid portion ρ_n move with a low velocity $\mathbf{v}$ and the superfluid portion ρ_s is at rest in the lab frame S, while in the frame S' moving with the walls the roles are reversed. Let $\hat{\mathbf{P}}$ denote the momentum operator. We have that in S' the walls are at rest, and so the Hamiltonian H_0 in this frame is independent of $\mathbf{v}$.

To proceed, it is easiest to work in the formalism of second quantization [46]. We introduce the creation and annihilation field operators $\hat{\psi}^\dagger(\mathbf{r}), \hat{\psi}(\mathbf{r})$ which create/destroy particles at positions $\mathbf{r}$, obeying the commutation relations

$$[\hat{\psi}(\mathbf{r}), \hat{\psi}^\dagger(\mathbf{r}')] = \delta(\mathbf{r} - \mathbf{r}') \tag{2.81}$$

$$[\hat{\psi}(\mathbf{r}), \hat{\psi}(\mathbf{r}')] = [\hat{\psi}^\dagger(\mathbf{r}), \hat{\psi}^\dagger(\mathbf{r}')] = 0 \tag{2.82}$$

Several important physical observables can then be expressed in terms of these field operators

$$\hat{N} = \int \mathrm{d}\mathbf{r}\, \hat{\psi}^\dagger(\mathbf{r})\hat{\psi}(\mathbf{r}) \tag{2.83}$$

$$\hat{\mathbf{R}} = \int \mathrm{d}\mathbf{r}\, \mathbf{r}\hat{\psi}^\dagger(\mathbf{r})\hat{\psi}(\mathbf{r}) \tag{2.84}$$

$$\hat{\mathbf{P}} = -i\hbar \int \mathrm{d}\mathbf{r}\, \hat{\psi}^\dagger(\mathbf{r})\nabla_{\mathbf{r}}\hat{\psi}(\mathbf{r}) \tag{2.85}$$

which are the number, many-body position, and total momentum operators respectively. In the frame S', the average total momentum is given by

$$\left\langle \hat{\mathbf{P}} \right\rangle_{S'} = \frac{1}{Z_0} \operatorname{Tr}\left(\hat{\mathbf{P}} e^{-\beta \hat{H}_0} \right) \tag{2.86}$$

where the partition function is given by $Z_0 = \operatorname{Tr}\left(e^{-\beta \hat{H}_0}\right)$. To go to the lab frame S, we need to boost from S' with velocity $-\mathbf{v}$. In non-relativistic quantum mechanics, boosts are Galilean transformations implemented via a unitary operator $\hat{U}$. Since we are not interested in time evolution, one has the freedom to set $t = 0$ and the operator is given by

$$\hat{U} = e^{-im\mathbf{v}\cdot\hat{\mathbf{R}}/\hbar} \tag{2.87}$$

describing a boost with velocity $\mathbf{v}$ and it can be verified that

$$\begin{aligned} \hat{U}^\dagger \hat{\mathbf{P}} \hat{U} &= \hat{\mathbf{P}} - m\mathbf{v}\hat{N} \\ \hat{U}^\dagger \hat{\mathbf{R}} \hat{U} &= \hat{\mathbf{R}} \end{aligned} \tag{2.88}$$

as expected. It is also useful to derive the Galilean transformation laws for the field operators using the Baker-Hausdorff lemma

$$\begin{aligned} \hat{U}^\dagger \hat{\psi}^\dagger(\mathbf{r}) \hat{U} &= \hat{\psi}^\dagger(\mathbf{r}) e^{i\frac{m}{\hbar}\mathbf{v}\cdot\mathbf{r}} \\ \hat{U}^\dagger \hat{\psi}(\mathbf{r}) \hat{U} &= \hat{\psi}(\mathbf{r}) e^{-i\frac{m}{\hbar}\mathbf{v}\cdot\mathbf{r}} \end{aligned} \tag{2.89}$$

In S the momentum is given by the inverse transformation $\hat{U}\hat{\mathbf{P}}\hat{U}^{\dagger}$. A key point is that $e^{-\beta\hat{H}}/Z$ is unchanged when switching between frames. Physically, it means that the probability distribution over states does not change if the system acquires a non zero center-of-mass velocity. This means that in the lab frame:

$$\left\langle\hat{\mathbf{P}}\right\rangle_S = \frac{1}{Z_0}\operatorname{Tr}\left(\hat{U}\hat{\mathbf{P}}\hat{U}^{\dagger}e^{-\beta\hat{H}_0}\right) = \frac{1}{Z_0}\operatorname{Tr}\left(\hat{\mathbf{P}}e^{-\beta\hat{H}_{\mathbf{v}}}\right) \tag{2.90}$$

where $\hat{H}_{\mathbf{v}} \equiv \hat{U}^{\dagger}\hat{H}_0\hat{U}$. The classical momentum of the normal portion is now equated with the thermal expectation of the momentum in the lab frame S, giving

$$\rho_n\Omega\mathbf{v} = \frac{1}{Z_0}\operatorname{Tr}\left(\hat{\mathbf{P}}e^{-\beta\hat{H}_{\mathbf{v}}}\right) \tag{2.91}$$

Later, we will make use of the identity

$$\nabla_{\mathbf{v}}\hat{H}_{\mathbf{v}} = i\frac{m}{\hbar}\hat{U}^{\dagger}[\hat{\mathbf{r}},\hat{H}_0]\hat{U} \tag{2.92}$$

The superfluid density can be related to the system's free energy in what follows, starting from the expression for the free energy in the lab frame

$$F_{\mathbf{v}} = -\frac{1}{\beta}\ln Z_{\mathbf{v}} \tag{2.93}$$

with $Z_{\mathbf{v}} = \operatorname{Tr}\left(e^{-\beta\hat{H}_{\mathbf{v}}}\right)$. If the Hamiltonian is separable into a kinetic and potential term: $\hat{H}_0 = \hat{T} + \hat{V}$ with $[\hat{V},\hat{\mathbf{r}}] = 0$ and $\hat{T}$ as the kinetic energy

$$\hat{T} = -\frac{\hbar^2}{2m}\int_{\Omega} \mathrm{d}\mathbf{r}\,\hat{\psi}^{\dagger}(\mathbf{r})\Delta_{\mathbf{r}}\hat{\psi}(\mathbf{r}) \tag{2.94}$$

Consequently, the commutator in (2.92) can be evaluated to give

$$\nabla_{\mathbf{v}}\hat{H}_{\mathbf{v}} = -\hat{\mathbf{P}} + m\mathbf{v}\hat{N} \tag{2.95}$$

This allows the momentum carried by the normal fraction of particles to be expressed in terms of the Hamiltonian and number operator. Substituting into Eq. (2.91) gives

$$\rho_n\Omega\mathbf{v} = -\frac{Z_{\mathbf{v}}}{Z_0}\nabla_{\mathbf{v}}F_{\mathbf{v}} + \frac{m\mathbf{v}}{Z_0}\operatorname{Tr}\left[\hat{N}e^{-\beta\hat{H}_{\mathbf{v}}}\right] \tag{2.96}$$

Taking the divergence of the above expression and then the limit that $\mathbf{v} \to 0$ yields a formula for the superfluid fraction

$$\rho_s = \frac{1}{\Omega d} \lim_{\mathbf{v} \to 0} \Delta_{\mathbf{v}} F_{\mathbf{v}} \tag{2.97}$$

and so the superfluid density is proportional to the Laplacian of the free energy in the zero velocity limit. Now let us assume that we are in the canonical ensemble such that the particle number is fixed: $[\hat{N}, \hat{H}_0] = 0$, meaning the partition function can be expanded in terms of N-particle position eigenstates $\{|\mathbf{R}\rangle\}$

$$Z_{\mathbf{v}} = \mathrm{Tr}\left[e^{-\beta \hat{H}_{\mathbf{v}}}\right] = \int \mathrm{d}\mathbf{R}_0\, \mathrm{d}\mathbf{R}_1 \cdots \mathrm{d}\mathbf{R}_{n-1} \prod_{j=0}^{n-1} \langle \mathbf{R}_j |\, e^{-\epsilon \hat{H}_{\mathbf{v}}}\, |\mathbf{R}_{j+1}\rangle \tag{2.98}$$

where $|\mathbf{R}_n\rangle \equiv |\mathbf{R}_0\rangle$. The action of $\hat{U}$ on a position eigenstate can be readily evaluated using the Galilean transformation law of the field operators

$$\hat{U}\,|\mathbf{R}\rangle = \hat{U} \prod_{j=1}^{N} \hat{\psi}(\mathbf{r}_j)\,|0\rangle = e^{i \frac{m}{\hbar} \mathbf{v} \cdot \sum_j \mathbf{r}_j}\,|\mathbf{R}\rangle \tag{2.99}$$

by commuting $\hat{U}$ across all the field operators, and of course assuming that $\hat{U}\,|0\rangle = |0\rangle$. Applying the definition $\hat{H}_{\mathbf{v}} = \hat{U}^{\dagger} \hat{H}_0 \hat{U}$ to the the integrand gives

$$\prod_{j=0}^{n-1} \langle \mathbf{R}_j |\, e^{-\epsilon \hat{H}_{\mathbf{v}}}\, |\mathbf{R}_{j+1}\rangle = e^{-i \frac{m}{\hbar} \mathbf{v} \cdot \sum_{j=1}^{N} (\mathbf{r}_j^{(n)} - \mathbf{r}_j^{(0)})} \prod_{j=0}^{n-1} \langle \mathbf{R}_j |\, e^{-\epsilon \hat{H}_0}\, |\mathbf{R}_{j+1}\rangle \tag{2.100}$$

where $\mathbf{r}_j^{(i)}$ refers to the position of the j-th particle in the i-th time slice. We have $|\mathbf{R}_n\rangle \equiv |\mathbf{R}_0\rangle$ which is saying the world lines must close onto themselves. But with periodic boundary conditions, this condition is satisfied by allowing the world line ends to be separated by a lattice translation vector

$$\sum_{j=1}^{N} \mathbf{r}_j^{(n)} - \mathbf{r}_j^{(0)} = \sum_{i=1}^{d} L_i W_i \mathbf{e}_i \tag{2.101}$$

where $\mathbf{e}_i$ is the standard basis vector in the i-th direction and W_i is an integer called the *winding number*, counting the net number of times that particle world lines cross the boundary normal to $\mathbf{e}_i$. Putting it all together, the lab frame partition function derives from a 'Fourier transform' of the world line probability distribution $\pi(\mathbf{X})$ in the moving frame

$$Z_{\mathbf{v}} = \int \mathrm{d}\mathbf{X}\, e^{-i\frac{m}{\hbar}\mathbf{v}\cdot\sum_{i=1}^{d} L_i W_i \mathbf{e}_i} \prod_{j=0}^{n-1} \langle \mathbf{R}_j | \, e^{-\epsilon \hat{H}_0} \, | \mathbf{R}_{j+1} \rangle = Z_0 \left\langle e^{-i\frac{m}{\hbar}\mathbf{v}\cdot\sum_{i=1}^{d} L_i \hat{W}_i \mathbf{e}_i} \right\rangle \tag{2.102}$$

where $\hat{W}_i$ is an operator taking on eigenvalues W_i when applied to sequences of position eigenstates (world lines) and the thermal average is performed in the moving frame S'. Finally, the lab frame partition function (2.102) can be substituted into the lab frame free energy (2.93) and compute the superfluid density from (2.97)

$$\rho_s = \frac{1}{\beta \Omega d} \left(\frac{m}{\hbar} \right)^2 \left\langle \left(\sum_{j=1}^{d} \hat{W}_j L_j \mathbf{e}_j \right)^2 \right\rangle \tag{2.103}$$

This is the well-known *winding number estimator* that is used for calculating the superfluid density during finite-temperature quantum Monte Carlo simulations. For a hypercubic container i.e. $\Omega = L^d$, the formula specializes to

$$\rho_s = \frac{L^{2-d}}{\beta d} \left(\frac{m}{\hbar} \right)^2 \left\langle \hat{\mathbf{W}}^2 \right\rangle \tag{2.104}$$

Eq. (2.104) implies that the superfluid fraction is related to fluctuations in the winding number, as for an isotropic system there is no preferred direction and hence $\left\langle \hat{\mathbf{W}} \right\rangle$ vanishes. In order for the winding number to fluctuate, a global update of the world line configuration $\mathbf{X}$ is needed. The only way to achieve this is if there is cross-linking from quantum exchanges to create a macroscopic chain spanning a simulation cell length. Thus, an estimated $N^{1/d}$ atoms need to be moved simultaneously for the winding number to change.

At zero-temperature however, the sampled paths cease to close onto themselves and so the relation with the winding number (2.101) does not hold anymore. Therefore, the superfluid estimator that is employed in the ground state projector methods discussed in Sections 2.4.1, 2.4.2 is a modification of Eq. (2.103). It can be derived simply by rewriting Eq. (2.101) in terms of the system's center-of-mass,

$\mathbf{R}_{\rm CM}(t) = \frac{1}{N}\sum_{i=1}^{N}\mathbf{r}_i(t)$, where we have identified the superscript index k in $\mathbf{r}_i^{(k)}$ with the imaginary-time index t to help clarify the notation

$$\sum_{j=1}^{N}\mathbf{r}_j^{(n)} - \mathbf{r}_j^{(0)} = N(\mathbf{R}_{\rm CM}(\beta) - \mathbf{R}_{\rm CM}(0)) \qquad (2.105)$$

where the distance $\mathbf{R}_{\rm CM}(\beta) - \mathbf{R}_{\rm CM}(0)$ has to be calculated without invoking periodic boundary conditions. Repeating the derivation with Eq. (2.105) instead of Eq. (2.101), the superfluid fraction becomes

$$\frac{\rho_s}{\rho} = \lim_{\beta\to\infty}\frac{N}{2d\lambda}\frac{\langle[\mathbf{R}_{\rm CM}(\beta) - \mathbf{R}_{\rm CM}(0)]^2\rangle}{\beta} \qquad (2.106)$$

where we have normalized by the total density ρ to get the dimensionless *superfluid fraction* and recall that $\lambda = \hbar^2/2m$ is the 'inverse' mass, having the interpretation as the diffusion constant from considering the Schrödinger equation in imaginary time. Now the superfluid fraction can be seen as the ratio of two diffusion coefficients: $\rho_s/\rho = \lambda_s/\lambda$ with λ_s being analogous to the long-time limit of the Einstein self-diffusion of a classical fluid $\langle x^2\rangle/2t$ [45].

2.6 Computational Implementation

Let us now discuss a few remaining details about the computational implementation of the algorithm we have introduced.

2.6.1 Boundary conditions

We will first discuss the role of the boundary conditions for the simulation cell. Since we are interested in bulk properties, we need some way to extrapolate the behavior of the systems we study to the limit of infinite system size. We want the boundary effects induced by having finite simulation cell to be immaterial towards the physics we are interested in. A popular remedy for this is to apply *periodic boundary conditions* (PBCs) to the simulation cell, which are depicted in Fig. 2.6.

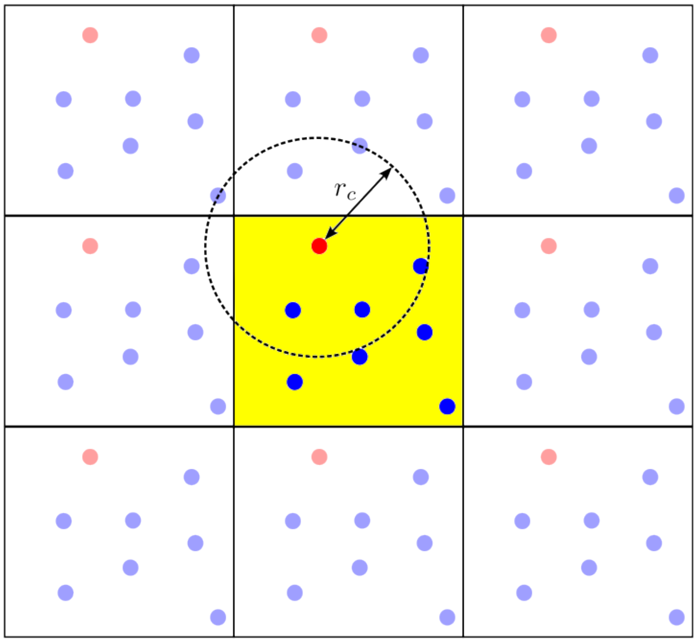

Figure 2.6: Schematic diagram of periodic boundary conditions, showing the main unit cell (center, in yellow), as well as the image cells obtained by translating the main cell by lattice vectors. A chosen reference particle is shown in red. The reference particle can interact with any other particle that falls within the cutoff distance r_c.

For convenience, let us assume that the system is enclosed inside a box with dimensions $L_x \times L_y \times L_z$. The way that PBCs work is that we take the main box as our unit cell, and surround it with repeating copies of itself, creating a tessellation over all space. Each particle in the main cell now has a 'periodic image' of itself in each of the cells, with each image particle position being the same as that of the main cell particle modulo translation by a lattice vector $\mathbf{R} = n_x L_x \hat{x} + n_y L_y \hat{y} + n_z \mathrm{L}_z \hat{z}$. Effectively, what we have done is endow the main simulation cell with the topology of a torus. Although PBCs do come with their own set of surface artifacts, they are normally much less severe than those without their prescription.

Now, the question becomes about how to handle particle interactions. In this work, we employ the *minimum image convention*, which is implemented through allowing particles to interact with other particles in different cells, but truncating the interaction potential at a cutoff radius r_c so that particles only interact with those within adjacent cells. We can do this because the interactions we will consider between particles in our systems are mainly short range, being zero to very good approximation at distances of order of the cutoff radius. We also require that $r_c < L/2$ where L is the smallest dimension of the simulation cell, so that particles do not interact with multiple periodic images of the same particle. However, applying a cutoff radius has unwanted effects on the computation of the system's energy since we are neglecting contributions coming from the 'tail' of the interaction potential. Therefore, we have to apply a correction to the final total energy based on these considerations, which we will derive in Appendix A for the helium-graphene system studied in Section 3.

2.6.2 Statistics

Just like with experiments in the real world, Monte Carlo simulations are subject to statistical noise, which has to be accounted for when interpreting the results obtained. Throughout a Monte Carlo simulation, we are making 'synthetic' measurements $x_1, ..., x_n$ of some fluctuating physical quantity X when the system is at thermal equilibrium, such as the energy. The best estimate of X given the available information is from taking the average over all the measurements

$$\bar{x} = \frac{1}{n}\sum_{i=1}^{n} x_i \tag{2.107}$$

for which we would like to assign an error. Let us model the consecutive measurements $x_1, ..., x_n$ as identical random variables. Computing the variance of the estimator $\bar{x}$ gives us

$$\sigma_{\bar{x}}^2 = \frac{1}{n}\left[A_0 + 2\sum_{t=1}^{n-1}(1 - t/n)A_t\right] \tag{2.108}$$

where we have exploited time-translation invariance in defining the autocorrelation function $A_t \equiv A_{ij}$ such that $t = |i - j|$, with A_{ij} being the covariance between x_i and x_j

$$A_{ij} = \langle x_i x_j \rangle - \langle x_i \rangle \langle x_j \rangle \tag{2.109}$$

Note that if the x_i's are independent i.e. $A_t = 0$ for $t > 0$, then Eq. (2.108) reduces to the commonly-used formula for the standard error in the mean

$$\sigma_{\bar{x}} = \sigma/\sqrt{n} \tag{2.110}$$

where σ is the standard deviation of the x_i's. The sample standard deviation can then be substituted into Eq. (2.110) as an estimate of the error. However, it is always the case that consecutive measurements are correlated with each other in Monte Carlo simulations, with the correlations decaying according to some characteristic time scale τ called the *correlation time*. By naively applying Eq. (2.110), we generally underestimate the error in $\bar{x}$ as we are overestimating the information content of our measurements.

One way to think about this is to imagine a random number generator which produces uniformly random integers between 0 and 10, with the twist that each randomly drawn integer is repeated k times before drawing the next. A sample output of this program could be for example: $1, 1, 1, 0, 0, 0, 5, 5, 5, 4, ...$ for $k = 3$. Suppose that the program generates a sample of size n. If n is significantly less than k, then the sample is likely to have variation, and we would be duped into thinking that the underlying distribution is narrow instead of being uniform. Therefore, we need more data points to see the true distribution emerge in the presence of correlations than without.

For measurements coming from Monte Carlo, the solution is to divide the data into n' equally-sized blocks of size B such that $n = n'B$ and compute the average of each block, obtaining a set of blocked values $x_1^{(B)}, ..., x_{n'}^{(B)}$, which we then use to compute the standard error. As shown in Ref. [49], the quantities $\bar{x}$ and $\sigma_{\bar{x}}^2$ are invariants with respect to the blocking transformation, and provided that A_t decays faster than $1/t$, A_t flows towards the fixed point $A_t \propto \delta_{0t}$ as B approaches τ, signalling the blocked variables becoming independent. For our concocted number generator, the blocked variables approach uniformity as $B \approx \tau = k$.

Chapter 3

Superfluidity of helium-4 films adsorbed onto graphene

3.1 Introduction

We now apply the framework developed in Section 2 to study the behavior of a helium-4 monolayer adsorbed onto a graphene substrate.

The first helium adlayer on graphene exhibits several equilibrium crystalline phases, which are classified as either *commensurate*, meaning the helium atoms are bound to specific adsorption sites in the graphene lattice, or *incommensurate*, meaning the helium crystal structure is independent of the underlying lattice. For the commensurate phases, it is common in the literature to see the notation C_n where 'C' stands for commensurate and n is the filling fraction of graphene adsorption sites that are occupied by a helium atom. As can be seen from Fig. 3.1, the first crystal phase that can be observed is the $C_{1/3}$ commensurate phase at coverage $\theta = 0.0636\,\mathring{A}^{-2}$, afterwards the system transitions through commensurate crystal phases of increasing filling fraction, separated by domain wall phases in-between, before finally transitioning to an incommensurate triangular crystal prior to the promotion of helium atoms to the second layer.

Our work is primarily aimed at addressing some existing controversy about whether a superfluid phase exists for $C_{1/3}$ helium-4 crystal adsorbed onto graphene, as several groups have obtained conflicting results. For instance, it was found through Diffusion

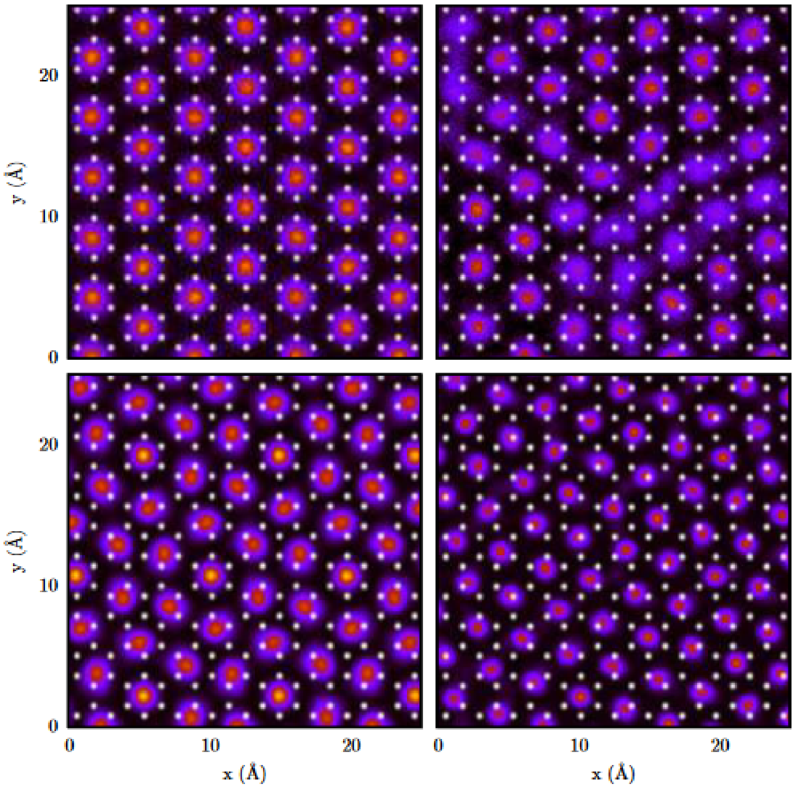

Figure 3.1: Density maps for different crystalline phases exhibited by a helium monolayer over graphene from quantum Monte Carlo simulations at temperature $T = 0.5$ K. *Top left:* $C_{1/3}$ commensurate phase at coverage $\theta = 0.0636$ $\AA^{-2}$. *Top right:* Domain wall phase at coverage $\theta = 0.072$ $\AA^{-2}$. *Bottom left:* $C_{7/16}$ commensurate phase. *Bottom right:* Incommensurate phase at coverage $\theta = 0.111$ $\AA^{-2}$, which is the max coverage prior to the promotion of atoms to the second layer. Reproduced from Ref. [50].

Monte Carlo (DMC) calculations by Gordillo and Boronat [27] that there is a small energy difference between the $C_{1/3}$ phase and a liquid phase, opening up the possibility of a metastable two-dimensional superfluid phase of helium-4. A follow-up DMC study by the same authors examined the prospect of first-layer supersolidity in closer detail, finding a small yet finite superfluid fraction ($\sim 0.67\%$) for the $C_{1/3}$ phase, growing to as high as 14% when vacancies are introduced [26]. On the contrary, Path Integral Monte Carlo (PIMC) simulations conducted by Kwon and Ceperly found zero superfluidity in the first layer for a perfect $C_{1/3}$ crystal when employing the same helium-carbon pair potential [28], with the same finding by Happacher et al.

using the continuous-space Worm algorithm [50].

Regardless, since the authors in Refs. [28, 50] simulated at finite temperature and made extrapolated predictions towards the ground state, one could argue that they did not reach the critical temperature for a superfluid signal to appear. When adsorbed onto the graphene, the helium atoms behave as a two-dimensional system, and so the superfluid transition is expected to conform with the Berezinskii–Kosterlitz–Thouless (BKT) paradigm [51], which predicts a universal jump in the superfluid density of two-dimensional fluids below a critical temperature [52]. The estimate of the superfluid fraction given in Ref. [27] yields a transition temperature of the order of 5 mK, which is below the temperature simulated by previous finite-temperature PIMC studies.

For zero-temperature methods like DMC however, this is not a concern. Thus, in our work we utilize a comparable methodology, the PIGS method from Section 2.4.1, which is also valid at $T = 0$ K. Additionally, we purposefully bias our calculation by using a trial wavefunction that is translationally invariant unlike in Refs. [26, 27], describing a state that is completely liquid despite us knowing a priori that the system forms a $C_{1/3}$ crystal at equilibrium. By doing so, we set at the beginning the most favorable conditions for possibly observing a metastable liquid state as described in [27], in search of a residual superfluid signal in the system's ground state.

3.2 Model and Methodology

3.2.1 Microscopic model

We consider an assembly of N helium atoms of mass m enclosed in a three-dimensional box with periodic boundary conditions, with the graphene substrate sheet the xy-plane. The following Hamiltonian constitutes the microscopic model of our system

$$\hat{H} = -\frac{\hbar^2}{2m}\sum_{i=1}^{N}\nabla_i^2 + \sum_{i<j} V_{\text{He-He}}(|\vec{r}_i - \vec{r}_j|) + \sum_{i,I} V_{\text{He-C}}(|\vec{r}_i - \vec{\ell}_I|) \tag{3.1}$$

featuring pairwise interactions between helium-4 atoms, as well as between helium-4 and carbon atoms. We simulate all the carbon atoms in a honeycomb lattice structure, retaining the full corrugation of the graphene substrate as opposed to approximating with a truncated Fourier expansion involving graphene reciprocal lattice vectors as in Ref. [53]. However, as a simplifying approximation, the masses of the carbon atoms were taken to be infinite so that they did not contribute to the kinetic energy. Although the mass of a lone carbon atom is only around 3 times that of a helium-4 atom, carbon atoms in the graphene sheet are stabilized by strong σ-bonds, and so it is an excellent approximation to treat them as static.

The helium-helium interaction potential was taken to be the Aziz potential [54]

$$\begin{aligned} V(r) &= \epsilon V^{\star}(x) \\ V^{\star}(x) &= A\exp\left(-\alpha x\right) - \left(\frac{C_6}{x^6} + \frac{C_8}{x^8} + \frac{C_{10}}{x^{10}}\right) F(x) \\ F(x) &= \begin{cases} \exp\left[-\left\{\frac{D}{x} - 1\right\}^2\right] & \text{for } x < D \\ 1 & \text{for } x \geq D \end{cases} \end{aligned} \tag{3.2}$$

with parameters $C_6 = 1.3732412$, $C_8 = 0.4253785$, $C_{10} = 0.1781$, $r_m = 2.9673$, $A = 544850$, $r_m = 2.9673$ and $\alpha = 13.353384$ such that $x \equiv r/r_m$. The helium-carbon interactions were modelled with the Lennard-Jones (LJ) potential

$$V_{\text{He-C}}(r) = 4\epsilon\left[\left(\frac{\sigma}{r}\right)^{12} - \left(\frac{\sigma}{r}\right)^{6}\right] \tag{3.3}$$

where σ and ϵ represent the hard-core distance and depth of the attractive well respectively. For consistency with previously performed calculations, we use the same LJ parameters as in Refs. [26, 27, 55, 56], which are $\sigma = 2.74\ \mathring{A}$ and $\epsilon = 16.25\ K$. To avoid the issues described in Section 2.6.1, cutoffs were applied to both potentials at $r_c = 14.75\,\mathring{A}$ and then smoothed to have vanishing derivatives $\frac{\mathrm{d}V}{\mathrm{d}r}\big|_{r=r_c} = 0$ at the cutoff distance. The correction to the energies due to having these cutoffs are derived in Appendix A.

Both potentials are quite similar in that they feature a combination of strong short distance repulsion (mainly from Pauli exclusion) and weak long distance Van der Waals attraction, which are prototypical for any kind of condensed matter interaction. They are also isotropic, depending only on the relative distance between particles. For the helium-helium interaction, this is justified by the spherical symmetry of the helium ground state. For the helium-carbon interaction however, it is less clear whether the assumption of isotropy is sensible. In their study of helium adsorption onto graphene, Kwon and Ceperly [28] also make use of an anisotropic pair potential determined to give better agreement with helium-graphite scattering data [57]. They assert that the monolayer properties at lower coverages $\theta < \theta_0$ are strongly dependent on whether the isotropic or anisotropic forms of the pair potential are employed, with the melting of the $C_{1/3}$ structure occuring with respect to decreasing coverage for the isotropic pair potential. We critically assess this claim in Section 3.4.1 in light of our own calculations at finite temperature.

The simulation cell dimensions were chosen to be $\Omega = L_x \times L_y \times L_z = 34.08\mathring{A} \times 29.51\mathring{A} \times 50\mathring{A}$. The size in the z direction L_z was chosen arbitrarily, simply large enough so that boundary effects in that direction became immaterial. However, L_x and L_y were important, corresponding with the dimensions of a carefully chosen graphene slice such that stitching together all the periodic images yields the correct honeycomb lattice, free of defects. The slice of graphene we used contained a total of 384 carbon atoms, with a carbon-carbon bond length of $a \sim 1.42\mathring{A}$. After fixing the graphene slice, the number of helium atoms was fixed to be $N = 64$ so that the resulting coverage was $\theta = \frac{N}{L_x L_y} = 0.0636\,\mathring{A}^{-2}$, when a $C_{1/3}$ commensurate crystal is expected to be formed.

The $C_{1/3}$ phase features the binding of helium atoms at the sites of a triangular lattice, having the primitive translation vectors

$$\mathbf{a}_1 = 3a\begin{pmatrix}-\sqrt{3}/2 & 1/2\end{pmatrix}^T, \quad \mathbf{a}_2 = 3a\begin{pmatrix}0 & 1\end{pmatrix}^T \tag{3.4}$$

The corresponding primitive vectors for the reciprocal lattice are then given by

$$\mathbf{b}_1 = \frac{4\pi}{3\sqrt{3}a}\begin{pmatrix}-1 & 0\end{pmatrix}^T, \quad \mathbf{b}_2 = \frac{4\pi}{3\sqrt{3}a}\begin{pmatrix}1/2 & \sqrt{3}/2\end{pmatrix}^T \tag{3.5}$$

which is another triangular lattice, but rescaled and rotated 90 degrees relative to the direct lattice. The first Bragg peak in the static structure factor will hence occur when $q = \frac{4\pi}{3\sqrt{3}a} \sim 1.7 \mathring{A}^{-1}$, which we will keep in mind for later.

The remaining details of the methodology are completely standard. We employed the fourth-order propagator (2.20) and performed convergence tests with respect to time step and projection time to calibrate our simulations. For the results involving the superfluid fraction, we used a time step of $\tau = \frac{1}{640}\, K^{-1}$, which was sufficient to see convergence of the superfluid fraction. However, it was necessary to go to a 10x lower time step to reach a convergent total energy. This is at least partially attributable to the kinetic term in the total energy, which as seen from the Euclidean action (2.17) is related to path curvature and hence needs smaller time steps to properly resolve, especially when there are 'kinks' in the world lines induced by short distance repulsion between atoms.

3.2.2 Details of Monte Carlo calculations

We used the Worm Algorithm to perform all finite temperature calculations based on the model (3.1) in the canonical ensemble (total number of particles N is fixed), for a temperature range of $T = 0.5$ K to 4 K. For our zero-temperature calculations, we used the PIGS algorithm, employing a Jastrow-type trial wavefunction

$$\psi_0(\mathbf{r}_1, ..., \mathbf{r}_N) = \exp\left[-\frac{1}{2}\sum_{i<j} u(|\boldsymbol{r}_i - \boldsymbol{r}_j|)\right] \tag{3.6}$$

embodying the pairwise correlations between helium atoms and the presence of a repulsive core, where the pseudopotential u is given by

$$u(r) = \frac{\alpha}{1 + \beta r^5} \tag{3.7}$$

with α and β as variational parameters to be adjusted in order to minimize the expected energy with respect to the trial wavefunction, finding $\alpha = 19$ and $\beta = 0.12\, \mathring{A}^{-5}$. The most important features of Eq. (3.6) are that it goes to zero for distances shorter than the hard-core distance, and saturates to a constant in the limit of large separation. Eq. (3.7) is a modification of the McMillan function $u(r) = (b/r)^5$ [58], where $e^{-u(r)}$ solves the two-body scattering problem for helium atoms at low energy.

Importantly, the trial wavefunction given in Eq. (3.6) is translationally invariant and contains no information about the underlying graphene lattice, unlike the choice in Refs. [26, 27], where solid order is built into their trial wavefunction by including one-body factors which localize particles within a horizontal layer above the substrate and at $C_{1/3}$ adsorption sites. Additionally, the trial wavefunction given in Eq. (3.6) is always positive and is thus guaranteed to have non-zero overlap with the true ground state (allowing it to be projected out), although one may expect that this would take an exceedingly long projection time because we haven't given the algorithm 'enough' physics at initialization. Assuming the claim made in Ref. [27] of the existence of a low-lying fluid state having a small energy difference compared to the ground state, one would also expect the system to remain disordered for a prolonged period as the algorithm tries to eliminate the fluid state's contribution. We wish to contest this scenario, which is the reason behind our choice of trial wavefunction.

For short projection times, the computed physical estimates reflect more of the trial wavefunction that was used as $e^{-\Lambda \hat{H}} \approx 1$. Since the trial wavefunction we utilize is oblivious to the presence of the substrate, there is no reason for helium atoms to remain close to the substrate at short projection times, and we would witness the evaporation of atoms off the graphene surface. This can be remedied by incorporating a one-body factor $\psi(z)$ in the trial wavefunction in a similar vein to what was done in Ref. [27]. In our work however, we simply relied upon the projection algorithm to stabilize the helium monolayer, finding projection times $\Lambda \geq 0.125\ \mathrm{K}^{-1}$ to be sufficient with no detectable evaporation.

3.3 Structure and energetics

As a test to see whether we could approach the regime where the ground state physics dominates, we computed system's total energy for a range of temperatures. Fig. 3.2 shows the total energy per helium-4 atom computed by the Worm Algorithm as a function of temperature. It can be seen that the energy estimates below $T = 1$ K are effectively constant, signalling that they can be treated as ground state estimates. Since the low energy (long wavelength) excitations of the two-dimensional helium film are phonons, the dominant term in the expansion of the energy is $\propto T^3$. Hence, we fit the purple data points in Fig. 3.2 with a cubic function $e_0 + \alpha T^3$, which is seen to have good agreement. Using the fit, we extrapolate to $T \to 0$ K, and read off a ground state energy per particle of $e_0 = -129.550(25)$ K. The ground state energy per particle from our PIGS calculations is $-129.49(7)$ K, so both our finite and zero temperature results are equivalent within error bars.

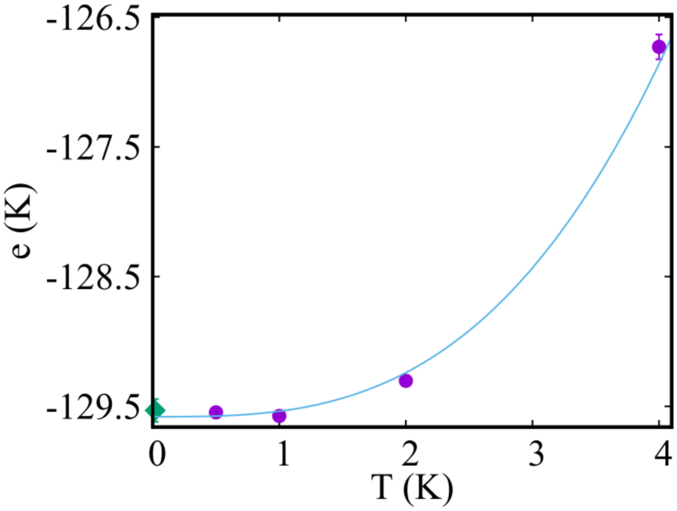

Figure 3.2: Energy per particle as a function of temperature The solid line is a fit of the form $e_0 + \alpha T^3$. Solid circles refer to results obtained from the finite temperature calculations. The estimate shown for $T = 0$ K (diamond) comes from our PIGS calculation with a projection time $\Lambda = 1$ K^{-1}; within its statistical uncertainty, this estimate is consistent with our zero-temperature extrapolation of finite-temperature estimates.

In contrast, Ref. [27] finds different values for the ground state energy per particle depending on the kind of trial wavefunction that is employed. From a trial wavefunction embodying translational invariance, i.e. one that is suitable for describing a liquid, they find a ground state energy per particle of $e_0 = -129.221(9)$ K. After incorporating *a priori* information about the $C_{1/3}$ crystal into the trial wavefunction, they find a slightly lower ground state energy per particle of $e_0 = -129.282(7)$ K. Based on the small energy gap of roughly 0.06 K that they found between a $C_{1/3}$ solid and liquid, the authors of Ref. [27] suggested that it pointed towards the existence of a metastable liquid phase that is energetically competitive with the insulating crystalline ground state.

Comparing with our result however, we find that the ground state total energy per particle we obtain is significantly lower (by ~ 0.3 K) despite utilizing identical pair potentials. The magnitude of this difference is three times than the solid-liquid energy gap reported in Ref. [27]. Our results show that in fact, the DMC method in Ref. [27] failed to reach the system's true ground state. The same observation has been made in the past [59], on account of issues with population size bias in DMC [41, 42], which typically make path integral approaches the more reliable option for studying properties of systems of bosons.

To quantitatively pinpoint the emergence of long-range crystalline order within the monolayer, we computed the static structure factor at the commensurate coverage $\theta = \theta_0$ for wave vectors $\mathbf{q}$ lying within the graphene plane, then rotationally averaged for expressing in terms of the magnitude q. The presence of solid order is evident by the Bragg peak at $q \sim 1.7$ Å^{-1} shown in the left of Fig. 3.3, consistent with the formation of a $C_{1/3}$ crystal. The right of Fig. 3.3 shows the density profile of the helium monolayer, which is the same as that obtained in previous Monte Carlo studies [27] and from solving the Schrödinger equation for particle moving transversely relative to the plane in an averaged substrate potential $V(z)$ [60].

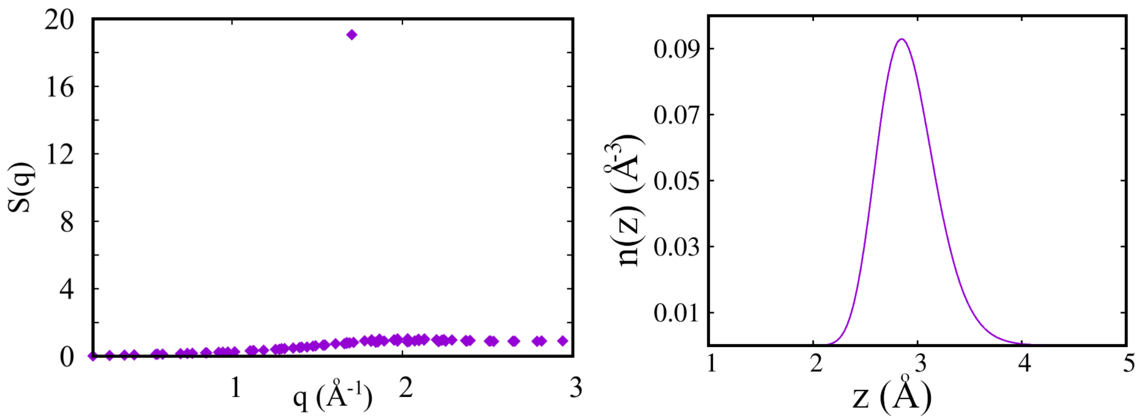

Figure 3.3: *Left:* Static structure factor $S(q)$ for an adsorbed film of ^{4}He on graphene, calculated at $T = 0.5$ K for wave-vectors lying within the plane of the graphene. There is a sharp peak in correspondence of q=1.7 Å^{-1}. *Right*: Average ^{4}He density as a function of the perpendicular distance from the graphene plane, computed at the same temperature.

3.4 Search for a metastable superfluid state

To search for a possible metastable superfluid state, we conducted the same computational experiment as in Refs. [61, 62]. Instead of a graphene substrate, helium-4 atoms were first simulated over a lithium substrate (modelled as a smooth, featureless plane due to the weakness of the lithium-helium interaction), maintaining the same coverage as before $\theta = \theta_0$, where it is known that the resultant helium film is nearly 100% superfluid [3]. Once it was confirmed that the system had equilibrated, an instantaneous snapshot of the helium world line configurations was taken. The lithium substrate was then replaced with the original corrugated graphene substrate and the simulation was resumed from the snapshot.

If a metastable superfluid state truly existed, then one might expect that the simulation would have trouble 'finding' the true crystalline ground state, requiring the disentanglement of global exchange cycles that give rise to the superfluid signal. Instead, what we find is that the exchange cycles disappear quite rapidly after transferring to the graphene substrate, with a resulting drop in the superfluid fraction.

On the left of Fig. 3.4a, nearly all of the particle world lines are cross-linked with

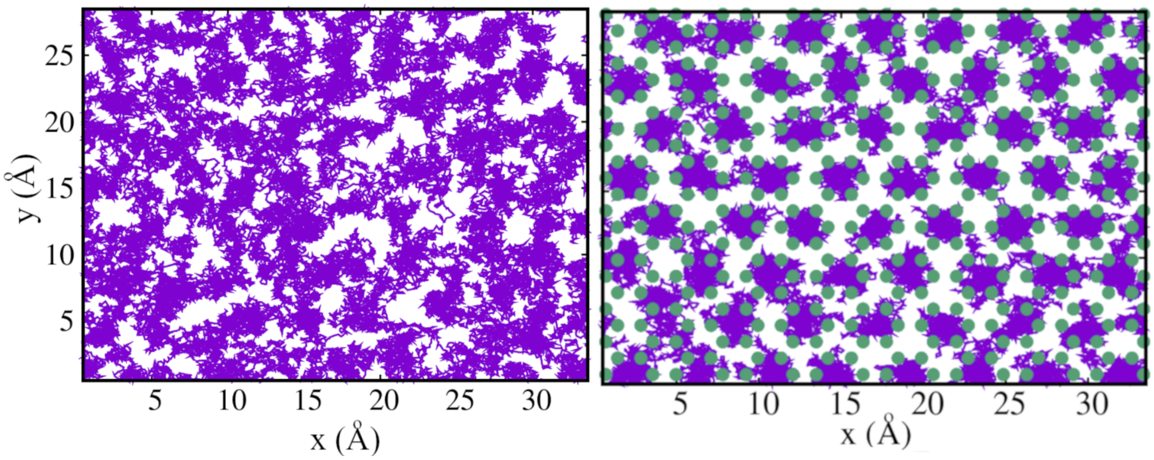

(a) World line configurations for lithium substrate (left) and graphene (right). Solid circles represent carbon atoms.

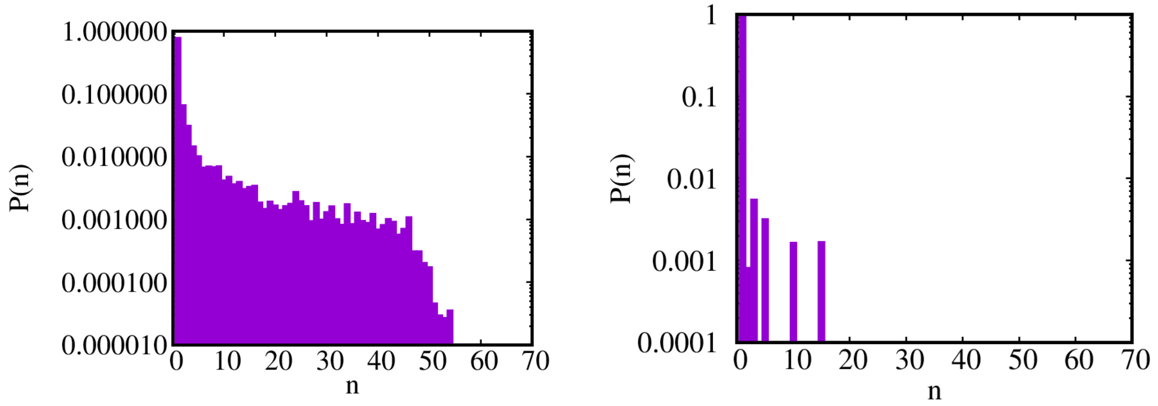

(b) $P(n)$ for lithium substrate.

(c) $P(n)$ for graphene

Figure 3.4: *Top*: Snapshots of world line configurations for lithium (top left) and graphene (top right) at $T = 0.5$ K. The system over lithium is almost entirely superfluid when the snapshot is taken, after which the substrate is replaced with graphene and crystalline order quickly emerges. *Bottom*: Histogram of exchange cycles involving n particles $P(n)$ for lithium (bottom left) and graphene (bottom right), at $T = 0.5$ K. Note that a logarithmic scale has been chosen for the y-axis. Upon transferring to graphene, the vast majority of sampled permutations are the identity permutation where the world lines are left as they are. The few remaining $n > 0$ cycles show up as isolated peaks in $P(n)$.

each other, forming macroscopic chains of exchanges spanning the entire lengths of the simulation cell. On the right panel, however, we see that these are broken down in the presence of the corrugated substrate, as the simulation algorithm continues to sample new configurations. A crystalline arrangement emerges with particle world lines localized in periodic fashion, with a few resilient exchange cycles remaining.

Such cycles can lead to a finite superfluid signal provided that the simulation cell is small enough (but we wish to point out that the superfluid signal is essentially not measurable in the configuration shown on the right part of Fig. 3.4a). However, we are skeptical that this effect persists in the thermodynamic limit. One way to tell is through monitoring the histogram $P(n)$ of exchange cycles involving n atoms. If $P(n)$ consists of a few isolated peaks, it is an indication that the sampling algorithm needs more run-time to remove those resilient cycles rather than a genuine superfluid signal. Indeed, this is what we observe in our $P(n)$ histogram from Fig. 3.4c, suggesting that there is no metastable superfluid phase. We revisit this point in Section 3.5.2 by conducting a similar experiment with the zero-temperature PIGS method, starting from a completely superfluid state and then projecting out the ground state in the presence of a corrugated graphene substrate.

3.4.1 Low coverage

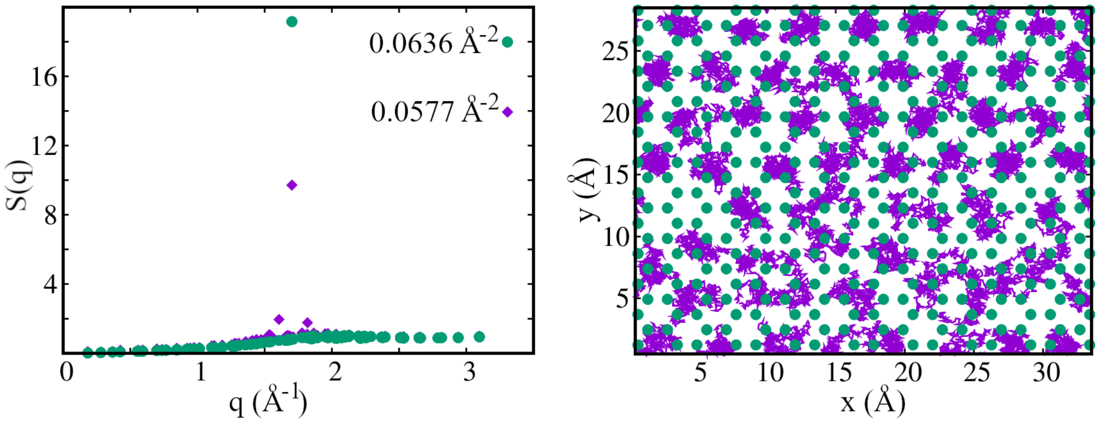

Figure 3.5: *Left:* Computed structure factor at $T = 1$ K at commensurate $\theta = 0.0636$ $\mathring{A}^{-2}$ coverage, as well as at a lower coverage $\theta = 0.0577\,\mathring{A}^{-2}$, at which it is argued in Ref. [28] to harbor a metastable superfluid state. *Right:* Snapshot of world line configuration at the lower coverage. Solid circles represent the carbon atoms.

In Ref. [28], a claim is made that if the isotropic pair potential is used, then the melting of the $C_{1/3}$ crystal to form a superfluid phase occurs when the coverage is lowered from $\theta = \theta_0$ to around $0.583\,\mathring{A}^{-2}$, which is grounded in the observation of a corresponding drop by half in the height of the Bragg peak. If on the other hand, the anisotropic LJ potential is used, then no appreciable change is observed. Based on this comparison, the authors of Ref. [28] conclude that the choice of pair potential for modelling the helium-carbon interactions greatly affects the physics of the system.

Our calculations at a coverage of $\theta = 0.0577\,\mathring{A}^{-2}$ indicate that this is not the case. As shown in Fig. 3.4.1, although there is a reduction in the strength of the peak, there is still solid order present as evident by its narrowness. Inspecting the world line configurations in the right panel of Fig. 3.4.1, we see indeed that $C_{1/3}$ solid order is maintained. Examining the histogram of exchange cycles in Fig. 3.6, very rarely do exchange cycles involving a significant number of particles ~ 10 get sampled. Even so, the computed superfluid fraction at low coverage is less than 10^{-5}, so these cycles do not actually yield a measurable superfluid response. Based on our results for the structure factor and superfluid fraction, we find that the $C_{1/3}$ crystal structure is maintained, and that there are no signs of a metastable fluid phase after doping the helium crystal with vacancies.

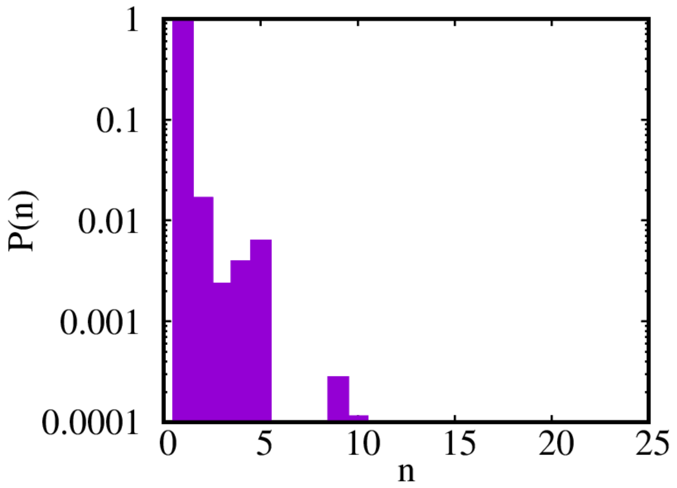

Figure 3.6: Histogram of exchange cycles involving n particles $P(n)$ for simulations at lower coverage $\theta = 0.0577\,\mathring{A}^{-2}$, with a logarithmic scale for the y-axis. Exchange cycles involving a finite number of particles are relatively infrequent, and do not induce a measurable superfluid signal ($< 10^{-5}$).

3.5 Zero temperature results

Our results at finite temperature suggest there is no metastable fluid, however, given a BKT scenario for the superfluid transition, we are still well above the predicted transition temperature of ~ 5 mK. We now present the results of our zero-temperature calculations using the PIGS method.

3.5.1 Structural properties

We start by discussing our results for the system's structural properties. Upon equilibration of the system in our PIGS simulations, a helium monolayer was formed, with an identical density profile as in our finite temperature calculations. Despite employing a trial wavefunction with no solid order built into it, we witnessed the development of long-range crystalline order, evident from the computed static structure factor shown in Fig. 3.7. This underlies an important methodological point; the PIGS algorithm is sufficiently reliable that it does not need to be hand-held, i.e. there is no need to add additional physics to it by incorporating the one-body factors in Refs.

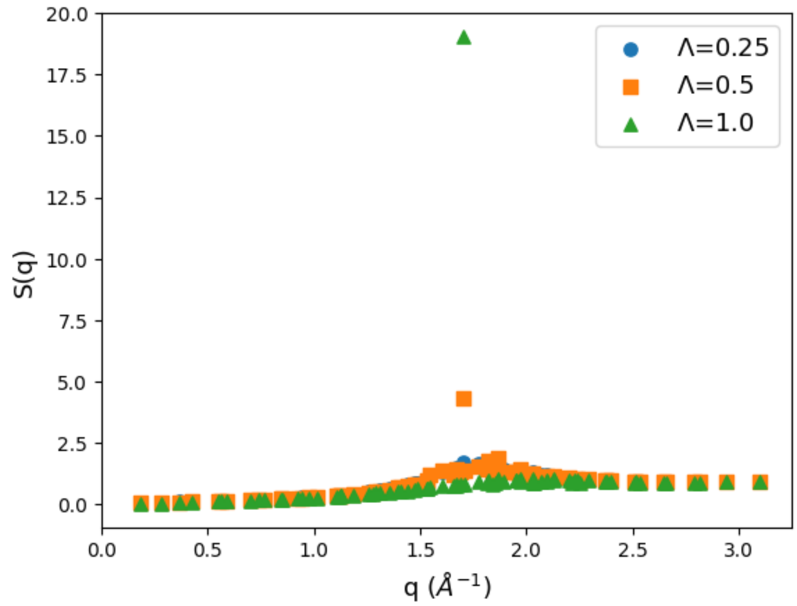

Figure 3.7: Static structure factor computed by PIGS as a function of projection time. The same Bragg peak at $q \sim 1.7 \AA^{-1}$ forms just as in our finite-T calculations.

[26, 27]. At lower projection times $\Lambda = 0.25$ K^{-1}, the system retains the liquid-like characteristics of the trial wavefunction. But as projection time is increased, a successively narrowing Bragg peak emerges at the expected location, agreeing with our results at finite temperature. Without much struggle, the projected out state breaks the translational symmetry of the trial wavefunction, with no signs of competition from a metastable fluid state.

3.5.2 Zero-temperature superfluid response

It is quite evident by now that the system's ground state is crystalline. Hence, we now set our sights on addressing the possibility of a small, non-zero superfluid fraction present in the $C_{1/3}$ phase reported in Ref. [26]. For the following discussion, we will write $\rho_S = \rho_s/\rho$ to simplify the notation. The superfluid fraction in PIGS is computed using the formula (2.106), which we reiterate below

$$\rho_S = \lim_{t\to\infty} D(t), \quad D(t) = \frac{N}{2d\lambda} \frac{\left\langle [\mathbf{R}_{\mathrm{CM}}(t) - \mathbf{R}_{\mathrm{CM}}(0)]^2 \right\rangle}{t} \tag{3.8}$$

where d is the dimensionality (set to be $d = 2$ because the helium layer is effectively two-dimensional) and $\mathbf{R}_{\mathrm{CM}}(t) = (1/N)\sum_{i=1}^{N} \mathbf{r}_i(t)$ with $\mathbf{r}_i(t)$ the position along the i-th world line at imaginary time t and $0 \le t \le \Lambda$. For a translationally invariant system, ρ_S is equal to 1.

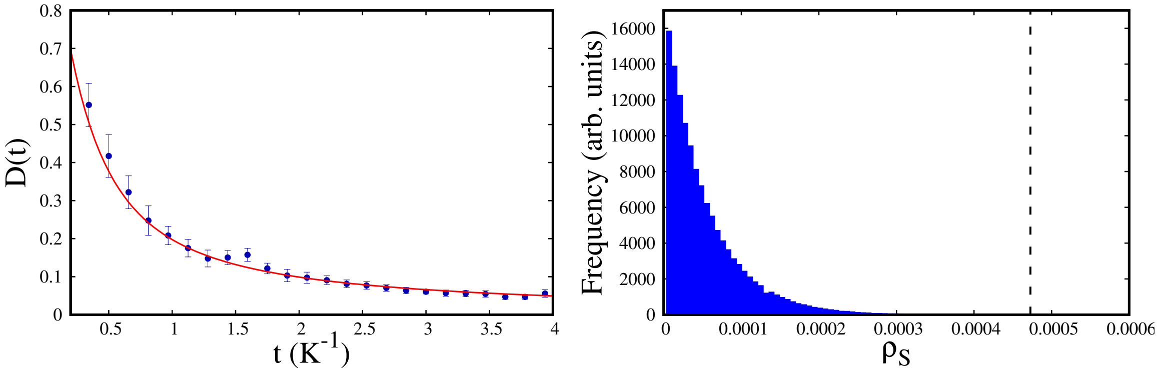

Figure 3.8: *Left:* Fit to the superfluid fraction curve at projection time $\Lambda = 4$ K^{-1} using Eq. (3.9). *Right:* Computed distribution of fit parameter ρ_S. The dotted line indicates the 99.99% confidence limit.

Since the world lines have finite length Λ, the center of mass still propagates out a finite distance, even if the distance in fact goes to zero in the infinite time limit. Therefore, we extract the asymptotic limit through fitting the diffusion curve $D(t)$ with the expression from Ref. [63]

$$D(t) = \rho_S + \frac{a}{t}\left(1 - e^{-bt}\right) \tag{3.9}$$

where ρ_S, a, and b are fitting parameters, ρ_S giving the extrapolated superfluid fraction in the infinite projection time limit. Such a formula was introduced without explanation in the original reference, but its use can be justified on the assumption of an Einstein-type diffusion behavior (i.e., with the diffusion coefficient $D(t) \propto 1/t$) for the normal (i.e., non-superfluid) component, which is expected to set in for a long time t, while for a short time the diffusion coefficient is expected to be mainly influenced by the trial wave function, and therefore should start out from some finite value. The form (3.9) simply interpolates between these two regimes.

We fit Eq. (3.9) to $D(t)$ through a Metropolis random walk over the space of parameters, obtaining the optimal fit parameters as well as their probability distributions for uncertainty estimates, the details of which are given in Appendix B. The fitting procedure is illustrated for $\Lambda = 4\ \mathrm{K}^{-1}$ in Fig. 3.8 and can be seen to be reliable over much of the domain.

Inspecting the distribution of ρ_S, we obtain an upper bound of $\sim 5 \times 10^{-4}$ on the superfluid fraction with 99.99% confidence, which is more than an order magnitude lower than the superfluid fraction reported in [26]. The fact that the superfluid fraction drops to an unmeasurably small amount during projection, despite starting from a translationally invariant, fully superfluid trial wave function, constitutes in our view strong evidence against the existence of superfluidity in the system's ground state.

We attribute the superfluid fraction ($\sim 0.67\%$) observed in Ref. [26] as likely being due to the population size bias issue mentioned in Section 2.4.2; specifically, the fact that one is working with a finite population of random walkers makes it impossible to remove completely the bias associated to the initial trial wave function, which has a nonzero superfluid component.

Chapter 4

Conclusions

In this thesis, we presented the results of our investigations into the physics of a helium-4 monolayer adsorbed onto graphene substrate, in search of a superfluid signal in its ground state.

In order to do so, we employed a powerful computational methodology: path integral Monte Carlo. We developed the background for this technique in Chapter 2 starting from quantum statistical mechanics, recasting the calculation of thermal expectation values as simple averages over imaginary-time paths that are statistically generated using the Metropolis algorithm. We showed how to incorporate the indistinguishability of particles through the sampling of permutations, reviewed zero-temperature variants of quantum Monte Carlo methods, and derived estimators for the calculation of different physical quantities such as the energy, pair distribution function, structure factor, and even superfluid fraction.

After developing the methodology, we applied it to our problem at hand, making use of both finite-temperature and zero-temperature quantum Monte Carlo simulations of a helium-4 monolayer over graphene. Through our finite-temperature calculations for the $C_{1/3}$ crystal phase, we obtained the system's equation of state as the total energy per particle as a function of temperature. We found a ground state energy significantly lower than the ground state estimate given in Ref. [27], with the magnitude of the difference three times greater than the proposed energy gap between the ground state and a metastable liquid state, indicating that the DMC procedure in Ref. [27] had not actually converged to the ground state, likely due to methodological issues with DMC such as population size bias.

To look for a metastable liquid state more directly, we conducted an experiment involving first running the simulation over a lithium substrate to produce a completely superfluid state and then swapping out the lithium for graphene. After the graphene is introduced, we found that the superfluidity dissipates quite rapidly, concurrent with the localization of world lines at $C_{1/3}$ adsorption sites. A few isolated exchange cycles remained, but the superfluid signal they induce is a finite-size effect as can be deduced from monitoring the histogram $P(n)$ of exchange cycles involving n particles.

We next addressed the claim raised in Ref. [28] that the system's physics depends heavily on the helium-carbon pair potential used for modelling their interactions, their evidence being that a liquid state is harbored at lower coverages $\sim$ 0.0583 $\mathring{A}^{-2}$ for the isotropic pair potential due to the destabilization of the $C_{1/3}$ structure from vacancy-doping, while this does not occur with the anisotropic potential. We simulated the system using the isotropic pair potential at a coverage $\theta = 0.0577$ $\mathring{A}^{-2}$ with even more vacancies present and computed the static structure factor. We indeed observed the same reduction of the $C_{1/3}$ Bragg peak as in Ref. [28], but the peak remains narrow and the system retains its crystalline character. We concluded that the physics remains essentially the same whether the isotropic or anisotropic forms of the He-C interaction are employed.

Finally, we performed simulations of the system at zero-temperature using the PIGS method, to see whether a small yet finite superfluid fraction exists for the $C_{1/3}$ phase as reported in Ref. [26]. To set up the most favorable conditions for superfluidity at the beginning, we employed a translationally-invariant trial wavefunction with no built-in information about the substrate. Nonetheless, through the PIGS projection algorithm we witnessed the development of $C_{1/3}$ crystalline order in the system with increasing projection time, providing further evidence against the existence of a low-lying liquid phase. To evaluate the presence of a ground-state superfluid response, we computed the superfluid fraction in our PIGS simulations by fitting the center-of-mass diffusion curve and extrapolating to the limit of infinite projection time, finding a negligible superfluid signal with a high degree of confidence.

Altogether, our calculations at finite and zero temperature agree with each other and provide strong evidence against the existence of a metastable superfluid phase, and that the ground state of a helium monolayer over graphene is indeed, an insulating $C_{1/3}$ crystal.

Bibliography

[1] P. Kapitza, *Nature*, vol. 141, 1938.

[2] J. F. Allen and A. D. Misener, *Nature*, vol. 141, 1938.

[3] M. Boninsegni, M. W. Cole, and F. Toigo, *Phys. Rev. Lett.*, vol. 83, 1999.

[4] M. Boninsegni and L. Szybisz, *Phys. Rev. B*, vol. 70, 2004.

[5] E. Van Cleve, P. Taborek, and J. E. Rutledge, *J. Low Temp. Phys.*, vol. 150, 2008.

[6] M. Bretz, J. G. Dash, D. C. Hickernell, E. O. McLean, and O. E. Vilches, *Phys. Rev. A*, vol. 8, 1973.

[7] G. J. Goellner, J. G. Daunt, and E. Lerner, *J. Low Temp. Phys.*, vol. 21, 1975.

[8] K. Carneiro, W. D. Ellenson, L. Passell, J. P. McTague, and H. Taub, *Phys. Rev. Lett.*, vol. 37, 1976.

[9] R. E. Ecke and J. G. Dash, *Phys. Rev. B*, vol. 28, 1983.

[10] S. E. Polanco and M. Bretz, *Phys. Rev. B*, vol. 17, 1978.

[11] P. A. Crowell and J. D. Reppy, *Phys. Rev. Lett.*, vol. 70, 1993.

[12] E. Cheng, W. F. Saam, M. W. Cole, and J. Treiner, *J. Low Temp. Phys.*, vol. 92, 1993.

[13] S. Moroni and M. Boninsegni, *Phys. Rev. B*, vol. 99, 2019.

[14] P. A. Crowell and J. D. Reppy, *Phys. Rev. B*, vol. 53, 1996.

[15] M. Neumann, J. Nyéki, B. P. Cowan, and J. Saunders, *J. Low Temp. Phys.*, vol. 138, 2005.

[16] M. Neumann, J. Nyéki, B. Cowan, and J. Saunders, *Science*, vol. 317, 2007.

[17] M. Neumann, A. J. Casey, L. V. Levitin, B. Cowan, and J. Saunders, *J. Low Temp. Phys.*, vol. 158, 2009.

[18] C. P. Lusher, B. P. Cowan, and J. Saunders, *Phys. Rev. Lett.*, vol. 67, 1991.

[19] A. Casey, H. Patel, J. Nyéki, B. P. Cowan, and J. Saunders, *Phys. Rev. Lett.*, vol. 90, 2003.

[20] H. Godfrin, R. R. Ruel, and D. D. Osheroff, *Phys. Rev. Lett.*, vol. 60, 1988.

[21] M. Siqueira, J. Nyéki, B. Cowan, and J. Saunders, *Phys. Rev. Lett.*, vol. 78, 1997.

[22] E. Collin, S. Triqueneaux, R. Harakaly, M. Roger, C. Bäuerle, Y. M. Bunkov, and H. Godfrin, *Phys. Rev. Lett.*, vol. 86, 2001.

[23] M. Boninsegni and N. V. Prokof'ev, *Rev. Mod. Phys.*, vol. 84, 2012.

[24] E. Kim and M. H. W. Chan, *Science*, vol. 305, 2004.

[25] P. Corboz, M. Boninsegni, L. Pollet, and M. Troyer, *Phys. Rev. B*, vol. 78, 2008.

[26] M. C. Gordillo, C. Cazorla, and J. Boronat, *Phys. Rev. B*, vol. 83, 2011.

[27] M. C. Gordillo and J. Boronat, *Phys. Rev. Lett.*, vol. 102, 2009.

[28] Y. Kwon and D. M. Ceperley, *Phys. Rev. B*, vol. 85, 2012.

[29] S. A. Chin, *Physics Letters A*, vol. 226, 1997.

[30] J. E. Cuervo, P.-N. Roy, and M. Boninsegni, *The Journal of Chemical Physics*, vol. 122, 2005.

[31] J. Cao and B. J. Berne, *The Journal of Chemical Physics*, vol. 97, 1992.

[32] S. A. Chin, *Phys. Rev. E*, vol. 71, 2005.

[33] N. Metropolis, *Los Alamos Science Special Issue*, vol. 15, 1987.

[34] J. Thijssen. *Computational Physics*, 2nd ed., Cambridge University Press, 2007.

[35] D. M. Ceperley, *Rev. Mod. Phys.*, vol. 67, 1995.

[36] M. Boninsegni, *J. Low Temp. Phys.*, vol. 141, 2005.

[37] Y. Yan and D. Blume, *J. Phys. B: At. Mol. Opt. Phys.*, vol. 50, 2017.

[38] M. Boninsegni, N. Prokof'ev, and B. Svistunov, *Phys. Rev. Lett.*, vol. 96, 2006.

[39] M. C. Gordillo and D. M. Ceperley, *Phys. Rev. B*, vol. 58, 1998.

[40] M. Boninsegni, N. V. Prokof'ev, and B. V. Svistunov, *Phys. Rev. E*, vol. 74, 2006.

[41] G. L. Warren and R. J. Hinde, *Phys. Rev. E*, vol. 73, 2006.

[42] M. Boninsegni and S. Moroni, *Phys. Rev. E*, vol. 86, 2012.

[43] S. Jang, S. Jang, and G. A. Voth, *The Journal of Chemical Physics*, vol. 115, 2001.

[44] J.-P. Hansen and I. R. McDonald. *Theory of Simple Liquids*, 4th ed., Oxford Academic Press, 2013.

[45] E. L. Pollock and D. M. Ceperley, *Phys. Rev. B*, vol. 36, 1987.

[46] V. G. Rousseau, *Phys. Rev. B*, vol. 90, 2014.

[47] H. E. Hall, W. F. Vinen, and D. Shoenberg, *Proceedings of the Royal Society of London. Series A. Mathematical and Physical Sciences*, vol. 238, 1997.

[48] F. S. Wells, A. V. Pan, X. R. Wang, S. A. Fedoseev, and H. Hilgenkamp, *Sci Rep*, vol. 5, 2015.

[49] H. Flyvbjerg and H. G. Petersen, *The Journal of Chemical Physics*, vol. 91, 1989.

[50] J. Happacher, P. Corboz, M. Boninsegni, and L. Pollet, *Phys. Rev. B*, vol. 87, 2013.

[51] J. M. Kosterlitz and D. J. Thouless, *J. Phys. C: Solid State Phys.*, vol. 6, 1973.

[52] D. R. Nelson and J. M. Kosterlitz, *Phys. Rev. Lett.*, vol. 39, 1977.

[53] M. E. Pierce and E. Manousakis, *Phys. Rev. B*, vol. 62, 2000.

[54] R. A. Aziz, V. P. S. Nain, J. S. Carley, W. L. Taylor, and G. T. McConville, *The Journal of Chemical Physics*, vol. 70, 1979.

[55] G. Stan and M. W. Cole, *Surface Science*, vol. 395, 1998.

[56] M. C. Gordillo and J. Boronat, *Phys. Rev. B*, vol. 81, 2010.

[57] W. E. Carlos and M. W. Cole, *Surface Science*, vol. 91, 1980.

[58] W. L. McMillan, *Phys. Rev.*, vol. 138, 1965.

[59] M. Boninsegni, *Phys. Rev. Lett.*, vol. 111, 2013.

[60] P. A. Whitlock, G. V. Chester, and B. Krishnamachari, *Phys. Rev. B*, vol. 58, 1998.

[61] M. Boninsegni, N. Prokof'ev, and B. Svistunov, *Phys. Rev. Lett.*, vol. 96, 2006.

[62] M. Boninsegni, *Phys. Rev. B*, vol. 97, 2018.

[63] S. Zhang, N. Kawashima, J. Carlson, and J. E. Gubernatis, *Phys. Rev. Lett.*, vol. 74, 1995.

Appendix A: Tail correction to total energy

We want to calculate the correction to the total energy due to imposing a cutoff radius r_c. For any pairwise interaction potential term, it was shown in Eq. (2.66) that the total energy per particle due to interactions is

$$\frac{\Delta V}{N} = \frac{\rho}{2} \int \mathrm{d}\mathbf{r}\, V(r) g(r) \tag{A.1}$$

where ρ is the density of atoms and $g(r)$ is the pair correlation function. Let us consider first the contribution coming from interactions between helium atoms. Since we are trying to include the contributions from all atoms outside the cutoff radius, we integrate over all space such that $r > r_c$. Additionally, assume that $g(r) \approx 1$ outside the cutoff radius and specialize to the two-dimensional case in light of the helium atoms forming an effectively two-dimensional layer at distance $d \approx 2.8\,\mathring{A}$ above the graphene plane. Thus, the correction has the formula

$$\left(\frac{\Delta V}{N}\right)_{\text{He-He}} = \pi\theta \int_{r_c}^{\infty} \mathrm{d}r\, r V_{\text{Aziz}}(r) \tag{A.2}$$

Evaluating this integral given the form of the Aziz potential in Eq. (3.2) then yields

$$\left(\frac{\Delta V}{N}\right)_{\text{He-He}} = \epsilon\pi\theta r_m^2 \left[\left(\frac{Ar_c}{\alpha r_m} + \frac{2A}{\alpha^3}\right) e^{-\alpha r_c/r_m} - \frac{C_6}{4}\left(\frac{r_m}{r_c}\right)^4 - \frac{C_8}{6}\left(\frac{r_m}{r_c}\right)^6 - \frac{C_{10}}{8}\left(\frac{r_m}{r_c}\right)^8\right] \tag{A.3}$$

which is of order ~ 0.01 K. Now consider the contribution coming from helium-carbon interactions, where we note that there is no $1/2$ factor as in Eq. $(A.1)$ because helium and carbon atoms are distinct from one another. The helium-carbon correction thus

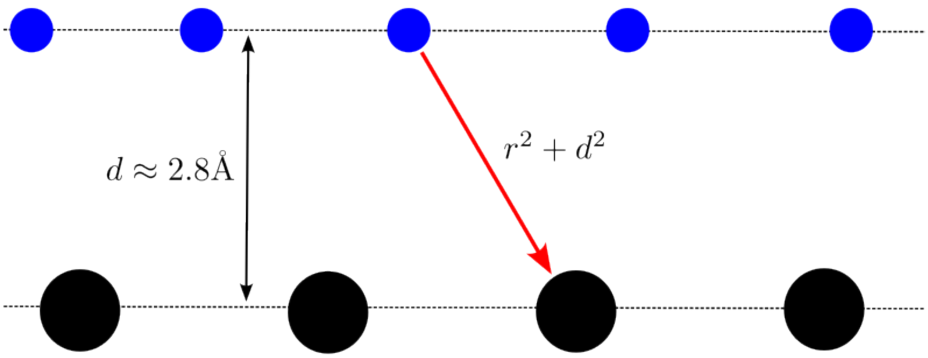

Figure A.1: Schematic diagram of computing the helium-carbon tail correction. We approximate the helium layer as a plane at distance $d = 2.8$Å from the substrate, neglecting zero-point motion in the transverse direction.

has the form

$$\left(\frac{\Delta V}{N}\right)_{\text{He-C}} = 2\pi\rho_c \int_{\sqrt{r_c^2-d^2}}^{\infty} \mathrm{d}r\, r V_{\text{LJ}}(\sqrt{r^2+d^2}) \tag{A.4}$$

where ρ_C is the density of carbon atoms in the graphene plane. Evaluating the integral using the form of the Lennard-Jones potential in Eq. (3.3) gives us

$$\begin{aligned}\left(\frac{\Delta V}{N}\right)_{\text{He-C}} &= 8\pi\epsilon\rho_C \int_{\sqrt{r_c^2-d^2}}^{\infty} \mathrm{d}r\, r \left[\left(\frac{\sigma^2}{r^2+d^2}\right)^6 - \left(\frac{\sigma^2}{r^2+d^2}\right)^3\right] \\ &= 2\pi\epsilon\sigma^2\rho_C \left[\frac{2}{5}\left(\frac{\sigma}{r_c}\right)^{10} - \left(\frac{\sigma}{r_c}\right)^4\right]\end{aligned} \tag{A.5}$$

Note that there is no dependence on the distance d of the film from the substrate unless the separation $d > r_c$, which is implausible given the density profile in Fig. 3.3. The density of carbon atoms in the plane is $\rho = N_c/L_xL_y \approx 0.38177\,\AA^{-2}$. Substituting in the values of the Lennard-Jones parameters, we obtain in the end a tail correction of size $\Delta V/N \approx -0.3485\,K$.

Appendix B: Details of Metropolis fitting

As discussed before, the superfluid fraction in PIGS can be calculated through the center-of-mass diffusion in imaginary-time $\mathbf{R}_{\mathrm{CM}}(t) - \mathbf{R}_{\mathrm{CM}}(0)$ without invoking PBCs, and taking the limit $t \to \infty$. We want to fit the diffusion curve in Eq. (3.8) with the fitting function given by (3.9), obtaining an estimate of ρ_S as well as its uncertainty induced by the noise present in Monte Carlo simulations.

To start, we estimate the fluctuation of each point in the diffusion curve by running J independent simulations simultaneously with identical parameters, obtaining at the end a set of diffusion curves $\{D_i(t)\}_{i=1}^{J}$. Then for each time value $0 \leq t \leq \Lambda$, we compute the blocked variables $\{D_i^{(B)}(t)\}_{i=1}^{K}$ over the dataset $\{D_i(t)\}_{i=1}^{J}$ where the block size is B and $J = BK$. Denote the average over the blocked variables as $\bar{D}(t) = \frac{1}{K}\sum_{i=1}^{K} D_i^{(B)}(t)$. It is clear that the block size does not affect the value of $\bar{D}(t)$, but gives us better control over the error. Indeed, by the Central Limit theorem, the blocked variables approach normally-distributed random variables centered at $\bar{D}(t)$. The sample standard deviation of the blocked variables $\delta D(t)$ then gives us an estimate of the Gaussian error bar for each point $\bar{D}(t)$.

We now apply a fitting procedure to the averaged curve $\bar{D}(t)$, using the obtained errors $\delta D(t)$ to inform the uncertainty estimates for the fitting parameters. Denote the set of fitting parameters as $\mathbf{\Omega} = \{\rho_S, a, b\}$ and the fitting function by $D_f(\mathbf{\Omega}, t)$. The probability of observing the datapoints $\{t_i, \bar{D}_i\}$ comprising $\bar{D}(t)$ as a function of the fitting parameters is then

$$P(\mathbf{\Omega}) = \prod_{\mathrm{i}} \frac{e^{-(\bar{D}_i - D_f(\mathbf{\Omega},t_i))^2/2\delta D(t_i)^2}}{\sqrt{2\pi\delta D(t_i)^2}} \tag{B.1}$$

which is a Gaussian distribution. Our goal is to perform maximum likelihood estimation of fitting parameters given this distribution. It can be seen that the maximum of Eq. (B.1) corresponds with fitting parameters which minimize the χ^2 statistic

$$\chi^2 = \frac{1}{K}\sum_{i=1}^{K}\left(\frac{\bar{D}_i - D_f(\mathbf{\Omega},t_i)}{\delta D(t_i)}\right)^2 \tag{B.2}$$

To estimate the optimal parameters, we perform a Metropolis random walk in the space of fitting parameters based on the distribution given in Eq. (B.1). This approach also grants access to the probability distributions of the fitting parameters, allowing for reliable estimation of parameter uncertainties.

During each step of the walk, a single component of $\mathbf{\Omega}$ is updated. Trial parameters $\mathbf{\Omega}'$ are proposed according to the rule

$$\Omega_i' = \Omega_i + (u - 1/2)\,\mathrm{d}\Omega_i \tag{B.3}$$

where Ω_i, Ω_i' are the i-th components of $\mathbf{\Omega}$ and $\mathbf{\Omega}'$ respectively, u is a uniform random number on $[0,1]$, and $\mathrm{d}\Omega_i$ is the magnitude of displacement which is tuned in order to maintain an acceptance rate for parameter updates of around forty to sixty percent. The acceptance probability $\mathbf{\Omega}_t \to \mathbf{\Omega}_{t+1} = \mathbf{\Omega}'$ according to the Metropolis recipe is then

$$P_{\text{acceptance}} = \min(1, P(\mathbf{\Omega}')/P(\mathbf{\Omega})) \tag{B.4}$$

Through performing the random walk, we obtain distributions for each fitting parameter from the visited values. In particular, the sample means and sample standard deviations of the distributions yield the optimal fitting parameters and uncertainty estimates respectively.